Journal of Structural Geology 177 (2023) 104986

Contents lists available at ScienceDirect

Journal of Structural Geology

journal homepage: www.elsevier.com/locate/jsg

Deformation and paleopiezometry of auriferous quartz veins in Archean orogenic gold deposits of the Abitibi greenstone belt

Crystal Brochard [*], Michel Jébrak, Stéphane De Souza

Université du Québec à Montréal, Geotop, 201 avenue du Président-Kennedy, H2X 3Y7, Montréal, QC, Canada

A R T I C L E I N F O

Keywords:
Quartz
Deformation
Recrystallization
Orogenic gold
Abitibi
Archean

A B S T R A C T

Most Archean orogenic gold deposits are associated with major faults such as the Larder Lake-Cadillac fault zone (LLCFZ) in the Superior craton and are hosted in or adjacent to second-order structures as quartz vein systems. Microstructures induced by quartz deformation in these faults or shear zones, such as typical textures of recovery and dynamic recrystallization, give indication of the P-T conditions during deformation. Electron backscatter diffraction (EBSD) analysis of grain lattice orientation and grain size determination, for flow stress calculation, are commonly performed on mylonite or quartzite samples from shear zones. This study tests the validity of such methods on hydrothermal auriferous quartz veins to better constrain the conditions of quartz vein deformation in the vicinity of the LLCFZ and evaluate the effect of depth and local variations on the microstructures and flow stress. Samples were collected in 24 gold deposits and showings along the LLCFZ. The microstructural observations and EBSD analysis allowed the distinction of six microstructural types within the studied samples. Samples analyzed with EBSD display a log-normal distribution of recrystallized grain sizes that is consistent with data for natural samples. The calculated flow stress is highly variable between samples and ranges from 38.2 + 5.1/-6.1 to 74.5 + 2.2/-3.0 MPa in surface samples only. Quartz recrystallization overprints primary textures in all but one samples, which indicates that recrystallization and its associated deformation occurred after the complete crystallization of the veins. Samples with bimodal distribution of recrystallized quartz grain sizes highlight the potential of quartz veins to record several deformation events. Samples are recrystallized at higher temperature and lower stress in the east than in the west of the LLCFZ, which could indicate the exposure of a deeper crust in the east. These data underline the potential of quartz vein microstructures to contribute to the evaluation and evolution of deformation conditions of auriferous quartz vein in an orogenic context.

1. Introduction

Quartz veins are common in many ore deposit types, including orogenic gold, porphyry, and epithermal deposits. In Precambrian greenstone belts, ore deposits are frequently overprinted by deformation and metamorphism that modify the primary textural and structural characteristics of quartz veins (e.g., White, 1943; Robert and Brown, 1986a,b; Robert and Poulsen, 2001). At a microscopic scale, the process of dynamic recrystallization (DRX) proceeds under various stress and temperature conditions during deformation and alters the texture (broad microstructural framework) of quartz veins (McCuaig and Kerrich, 1998; Stipp et al., 2002a, 2002b). This phenomenon is common in metamorphic rocks, and as documented in auriferous quartz veins of the Val-d'Or area (Boullier and Robert, 1992; Neumayr et al., 2000), throughout the Abitibi (Tuba et al., 2021) and Swayze greenstone belts (White, 1943), it impacts the evolution of quartz from orogenic gold deposits, which are commonly formed in metamorphic terranes (McCuaig and Kerrich, 1998; Goldfarb et al., 2005). Recent studies also highlighted the impact of aseismic deformation during the development of an orogenic gold system (Hunter et al., 2021) and post-formation processes such as pressure solution on gold morphology and distribution in veins (e.g., Fougerouse et al., 2016).

The recrystallized grain size of quartz is related to the flow stress during deformation in experimental and natural conditions (Twiss, 1977; Stipp et al., 2002a; Stipp and Kunze, 2008). This relationship allows to determine a reliable recrystallized grain size piezometer for quartz, and to calculate the differential stress or flow stress at the time of rock deformation (Stipp and Tullis, 2003; Stipp et al., 2010). The electron backscattered diffraction analysis (EBSD) was developed extensively in the past 20 years to study the DRX processes and textures in

* Corresponding author. 201 avenue du Président-Kennedy, H2X 3Y7, Montréal, QC, Canada.
E-mail addresses: brochard.crystal@courrier.uqam.ca (C. Brochard), jebrak.michel@uqam.ca (M. Jébrak), de_souza.stephane@uqam.ca (S. De Souza).

https://doi.org/10.1016/j.jsg.2023.104986
Received 20 April 2023; Received in revised form 17 October 2023; Accepted 20 October 2023
Available online 30 October 2023

deformed rocks and minerals (Adams et al., 1993; Trimby and Prior, 1999; Prior et al., 2009), recently focusing on quartz-rich rocks, quartz in mylonites (e.g., Behr and Platt, 2011) and quartz veins (e.g., Price et al., 2016; Lychagin et al., 2020) in shear zones. The EBSD analysis allows the distinction between relict grains, subgrains and newly recrystallized grains by identifying their crystallographic preferred orientation, and by the production of high-resolution lattice orientation maps (e.g., Cross et al., 2017). It also allows an objective and systematic analysis of microstructures and of the controlling DRX mechanism in deformed rock samples (e.g., Halfpenny et al., 2012). The calibration of a recrystallized grain size piezometer based on the EBSD analysis also allows for a rapid determination of the recrystallized grain size and the flow stress values (Cross et al., 2017). However, few studies focus on the micro-scale deformation of mineralized quartz veins with this approach (Hunter et al., 2021; Tavares Nassif et al., 2022).

This study focuses on the description of microstructures and the application of EBSD analysis on recrystallized quartz veins from 24 orogenic gold deposits and showings that were sampled along, or in the vicinity of the Larder Lake-Cadillac fault zone (LLCFZ), from Louvicourt (QC) to Kirkland Lake (ON) in the Archean Abitibi greenstone belt of Canada (Fig. 1). The aim of this study is to determine which types of DRX textures are found in hydrothermal orogenic quartz veins, the range of temperature at which it occurred, as well as an estimate of the flow stress during vein deformation. The study tests the EBSD analysis and the recrystallized quartz grain size piezometer calibrated by Cross et al. (2017) on hydrothermal quartz veins, and determines if the micro-structures and grain size are impacted by certain parameters, including local folding and sample depth. The microstructures and the flow stress values are compared to those found in metamorphic rocks, and implications on the timing of deformation and the regional setting are discussed.

2. Geological setting

The LLCFZ is a crustal-scale structure, a 10–600 m wide high strain zone that extends from Matachewan (ON) to Louvicourt (QC) over a strike length of about 250 km (Fig. 1). In Québec, this structure marks the limit between the Abitibi and the Pontiac subprovinces (Card, 1990; Daigneault et al., 2002). The LLCFZ consists of several segments defined by variations in its strike, dip, and expression of deformation (Bedeaux et al., 2017 and references therein; Poulsen, 2017). It is characterised by an early dip-slip movement and late dextral strike-slip shearing, but the sense of shear varies locally with the orientation of fault segments (Benn and Peschler, 2005; Bedeaux et al., 2017). Within the LLCFZ lies a discontinuous unit mainly represented by variably strained ultramafic to intermediate volcanic rocks and talc-chlorite ± carbonate-fuchsite schist, defined as the Piché Group or the Piché Structural Complex in Quebec (Bedeaux et al., 2018), or as a slice of the Tisdale assemblage in Ontario (Ispolatov et al., 2008). These rocks host some of the orogenic gold deposits located south of Rouyn-Noranda (Lac Gamble, Augmitto, Astoria, Cinderella; Fig. 1), as well as the Cheminis, Kerr Addison-Chesterville and McBean deposits in Ontario (Ispolatov et al., 2008; Lafrance, 2015).

The formation of the LLCFZ is attributed to underthrusting of the Pontiac Subprovince greenschist to amphibolite facies metasedimentary rocks below the southern Abitibi Subprovince greenschist facies supra-crustal rocks, prior to the deposition of the Timiskaming assemblage (Mueller et al., 1996; Daigneault et al., 2004; Bedeaux et al., 2017). The first post-Timiskaming main deformation event that affected the LLCFZ was associated with regional N–S shortening constrained between ca. 2669 and 2642 Ma (Dubé and Mercier-Langevin, 2020), and recorded as a penetrative east-west-trending schistosity (Wilkinson et al., 1999; Bedeaux et al., 2017). This event likely reactivated and linked earlier structures, allowing fluid channeling and crystallization of

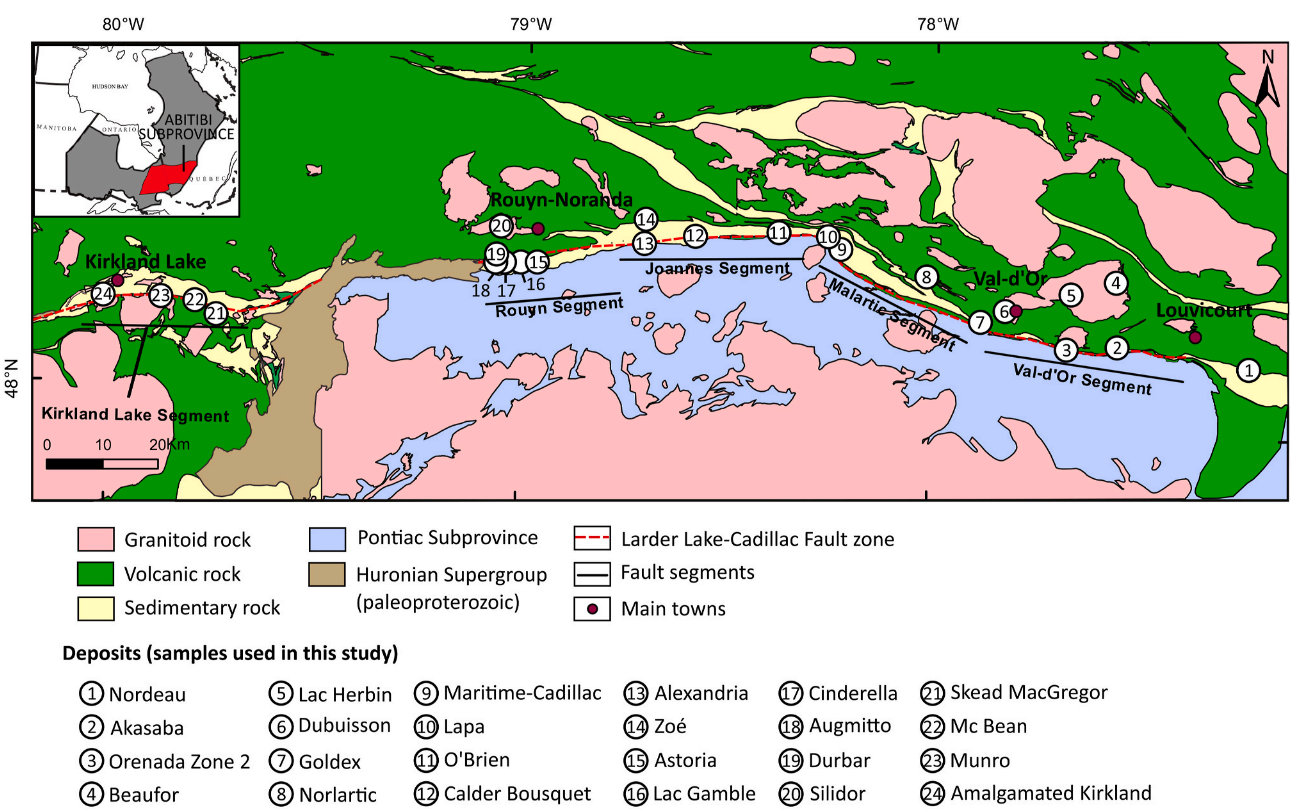

Fig. 1. Simplified geological map of the study area, with localization of samples, the LLCFZ and its different segments, as well as some of the main towns between the Val-d'Or and Kirkland Lake mining camps. Insert in left top corner localize the Abitibi Subprovince within the Superior Province. Modified from Bedeaux et al. (2017) and Poulsen (2017).

quartz-carbonate veins, as well as metasomatism in the adjacent rocks. This deformation event is associated with the regional low-pressure regional metamorphism described by Powell et al. (1995), that has been dominant in this southern part of the Abitibi subprovince (Wilkinson et al., 1999; Daigneault et al., 2002). Metamorphic contrasts are observed between the eastern and western parts of the LLCFZ and its vicinity, as upper greenschist grade rocks are found in the Val-d'Or area and subgreenschist to greenschist grade rocks in Rouyn-Noranda and Kirkland Lake (Powell et al., 1995; Ispolatov et al., 2008; Faure, 2015).

In the southern Abitibi Subprovince, numerous gold deposits of various types are found in the vicinity of the LLCFZ (e.g., Robert et al., 2005; Poulsen, 2017). The formation of the lode gold deposits and associated synorogenic quartz-carbonate veins along the LLCFZ are intimately associated with its deformation history between ca. 2692 Ma to 2660 Ma (Robert et al., 2005 and references therein). At least two vein generations and related mineralizing events are documented in the Val-d'Or district (Couture et al., 1994), including extensional and fault-fill or shear vein arrays (Robert and Brown, 1986a). Some of the documented shear veins exhibit textures typical of DRX, either partially or completely overprinting the primary textures (Robert et al., 1995; Robert and Brown, 1986b). According to Dubé and Mercier-Langevin (2020), the majority of the quartz-carbonate vein deposits in the Abitibi greenstone belt are syn-to late-deformation with respect to the main phase of post-Timiskaming shortening, and display overlapping mineralization styles.

3. Analytical methods

3.1. Sample selection

The materials used for this study are hydrothermal quartz veins from orogenic gold deposits. More than 30 samples were collected from 24 deposits and showings in the Val-d'Or, Rouyn-Noranda, and Kirkland Lake mining camps, in the vicinity of the LLCFZ (Fig. 1, Table 1). The aim of the sampling was to have a good representation of microstructures at surface and at depth along a corridor following the LLCFZ and to verify the influence of sample depth and folding on the DRX, recrystallized grain size and calculated flow stress. The samples were collected from outcrops, drill cores and underground mines (Fig. 2). The sample depth (Table 1) for drill hole samples was corrected by using the drill hole dip.

The outcrop samples from the Dubuisson property (Fig. 1, Table 1) were oriented to monitor the effects of thin section orientation and asymmetric folding on the quantification of quartz microstructures and on the calculated flow stress values. Three orthogonal thin sections were cut from the MET1 sample and two from the MET2 sample (Fig. 3). Thin section planes were defined with X, Y and Z axes; the Y axis being parallel to the strike of the shear zone that hosts the quartz vein (250°N, Fig. 3). The MET3 sample was oriented perpendicular to the fold axis (270°N), in the hinge of the main folded vein at the Dubuisson property.

Thin sections used for microstructural description and EBSD analysis are 30 μm thick polished thin sections prepared at the Colorado School of Mines Thin Section Laboratory (USA). Twenty samples exhibiting DRX were selected for the EBSD analysis. Optical microscopy was used to document microstructures and identify the dominant recrystallization mechanism, and to establish the minimum recrystallized grain size prior to EBSD analysis.

3.2. Microstructural descriptions

The microstructural observations and the interpretation of DRX mechanisms were made following the definitions of Drury and Urai (1990), Trimby et al. (1998) and reviews of Stipp et al. (2002a, 2002b) among others. Three recrystallization mechanisms intervene during DRX, namely bulging (BLG), sub-grain rotation (SGR), and grain boundary migration (GBM), depending on the temperature and strain conditions, and each one is characterized by specific microstructures (see White, 1976; Gifkins, 1994; Stipp et al., 2002a, b; Stipp and Kunze, 2008; Platt and Behr, 2011). Modification of quartz texture can also occur post-deformation by static recovery and recrystallization (Gottstein and Mecking, 1985; Bestmann et al., 2005). The grain size is defined as the diameter of a circle having the same surface area as the grain (e.g., Lopez-Sanchez and Llana-Fúnez, 2015). In the microstructural descriptions, the arithmetic mean of the grain size was calculated using optical measurements.

3.3. EBSD analysis

The 30 μm polished thin sections were prepared with a regular 1 μm polishing diamond paste and a 0.005 μm colloidal alumina polish was used to remove any mechanical damage caused by the diamond paste finish. A $<$ 5 nm carbon coating was applied on the polished thin sections to prevent the sample charging effect during the Scanning Electron Microscope (SEM) imaging (Lloyd, 1987; Trimby and Prior, 1999). EBSD analyses were performed on a Hitachi SU8230 SEM at the École de Technologie Supérieure (ÉTS) in Montreal (Canada). The EBSD data were collected using a 25 kV accelerating voltage and a 25 μA emission current. The working distance was fixed between 20 and 14.5 mm depending on the area of the thin section analyzed. The EBSD patterns were collected on a Brucker eFlash HR detector, processed and indexed using the Bruker Esprit software 2.2 version. The samples used for this study vary in terms of texture and grain size, so the step size was set according to the minimum recrystallized grain size in each sample ($\leq$1/5 of the smaller grain size, see Cross et al., 2017), and adapted during a pre-scan of the area with a larger step size. In the majority of samples, several maps were performed to ensure statistical significance. Following the recommendations of Lopez-Sanchez (2020), the samples with more than 427 grains are considered statistically significant. This value corresponds to a lognormal distribution of the grain size with a multiplicative standard deviation (MSD) of 1.7 and a 5% error margin, which appears to fit most of the data from this study (see Lopez-Sanchez, 2020).

Overall, the EBSD orientation maps obtained from hydrothermal quartz are of good quality. The indexing rate of the EBSD analyses was between 67.1% and 95.5% for all samples with an average of 85%, and non-indexed pixels represented between 25.8% and 5.01% of the map surface. However, the indexing rate can be increased when secondary phases are indexed, such as calcite. For example, calcite accounted for as much as 22.5% of the MCAD4 sample map. For most samples, the non-indexed pixels represented less than 10% of the map. For more details on the data quality, limitations, and recommendations on the application of the method on hydrothermal quartz veins, see Brochard (2022). The detailed EBSD results are included in the supplementary material of this paper, and full dataset available on demand.

3.4. Paleopiezometry

The raw EBSD orientation data were processed using the MTEX Matlab add-on (Bachmann et al., 2010, 2011; https://mtex-toolbox.github.io/). A misorientation of 10° was used as a threshold between low-angle and high-angle boundaries, defining the grain boundaries (Shigematsu et al., 2006). The Matlab code from Cross et al. (2017) was used to properly separate relict and recrystallized grains, and was adapted to the data in order to overcome some issues encountered during the post-processing. The internal deformation of individual grains was quantified by calculating the misorientation between each pixel and the mean orientation of the grain (Mis2Mean), which allows to differentiate between relict deformed grains and strain-free recrystallized grains. The modified Matlab code is provided in the Supplementary Data. Following recommendations of Lopez-Sanchez (2020) for a lognormal distribution of recrystallized grain size, the geometric mean of the grain size determined from the EBSD analysis was used in the

Table 1
Sample summary with coordinates in UTM NAD83 (Z18N), sample origin, host rock, thickness, and selected references for each showing or deposit.

LLCFZ Segment	Sample	Deposit/Showing	UTM coordinates		Mine level/Drill hole, z (m)	Host rock	Vein thickness (cm)	Vein mineralogy	Vein type	Structural control	Ref.
			Easting	Northing							
Val-d'Or	NORD40	Nordeau West	333128.0	5319850.0	PG-06-07, 450	Greywacke	–	Qz-Cb	u	Local shear	Langton and Horvath (2009), Langton and Ladid (2019)
	AKA54	Akasaba West	309173.0	5324659.0	IAX-11-132, 45	Felsic crystal tuff	1–1.5	Qz-Cb(Cal)	u	–	Beauregard et al. (2012)
	OREN58	Orenada zone 2	299079.0	5325349.0	AAX-07-10, 260	Siltshale	–	Qz-Ank-Tur	u	finely folded	Neumayr et al. (2000), Savard et al. (2018)
	BEAU10	Beaufor	309977.0	5336978.0	N355(SN 22C), 108	Granodiorite	–	Qz-Cb ± Tur	e	sheared	Rezeau et al. (2017), Tremblay et al. (2020)
	HERB73	Lac Herbin	300471.0	5334719.0	N15 (Ga. L, WE zone)	Granodiorite	–	Qz-Tur ± Cb	e	–	Lemarchand (2012), Tremblay et al. (2020)
	DUB16	Dubuisson	288877.0	5328952.0	Outcrop, vein border	Intrusive PB	–	Qz-Cb	s	in E-W shear zone	Barbe (2011)
	DUB17		288877.0	5328952.0	Outcrop, vein #5	Intrusive PB	–		s	in E-W shear zone	Barbe (2011)
	MET1		289375.0	5332311.0	Outcrop, 3D test	Intrusive PB	52.6	Qz	s	in E-W shear zone	Barbe (2011)
	MET2		289375.0	5332311.0	Outcrop, small vein	Intrusive PB	3.5	Qz	s	in E-W shear zone	Barbe (2011)
	MET3		289461.0	5332307.0	Outcrop, fold hindge	Intrusive PB	35.6	Qz	s	fold hinge	Barbe (2011)
	GOLD2-1	Goldex	286731.3	5330588.6	GD37-040, 261	Granodiorite	2.5	Qz-Cb-Tur	u	–	Genest et al. (2012), Munger (2019)
	GOLD2-2		286731.3	5330588.6	GD37-040, 261	Granodiorite	4	Qz-Cb-Tur	u	–	Genest et al. (2012), Munger (2019)
	GOLD1		286331.3	5330569.6	65-031, 671	Granodiorite	6	Qz-Tur	u	–	Genest et al. (2012), Munger (2019)
	GOLD3		286960.9	5330787.1	GD128-024, 1493	Diorite	8	Qz	u	–	Genest et al. (2012), Munger (2019)
Malartic	NORL46	Norlartic	277471.0	5337214.0	NL-11-040, 26	Quartz diorite	Stockwork	Qz-Cb	u	–	Belzile (2016)
	MCAD4	Maritime-Cadillac	257022.0	5344935.2	141-18-38, 36	Basalt	2.3	Qz-Cb	u	weak foliation	Bernard (2018)
	MCAD6		257022.0	5344935.2	141-18-38, 169	Basalt	5.7	Qz-Cb	u	–	Bernard (2018)
	MCAD82		256963.8	5345704.3	141-10-23, 280	Tonalite	0.4	Qz	u	weak foliation	Théberge (2011)
	MCAD2		256926.5	5344945.7	141-18-39, 453	Basalt	5	Qz-Cb	u	weak foliation	Bernard (2018)
Joannes	LAPA75	Lapa	256136.0	5346791.0	LA06-49-08, 1120	Bt-(Chl) Schist	0.3	Qz	u	–	Simard et al. (2013)
	OBR66, 67	O'Brien	247281.0	5347921.0	Unknown depth	Polygenic conglo.	–	Qz-Cb	u	–	Beausoleil (2018)
	CALD48	Calder Bousquet, Zone 2	232828.2	5348108.6	BO-10-03, 147	Greywacke	>50[a]	Qz-Ank -Tur	u	folded host rock	Kramo (2017)
	ZOE19	Zoé	224040.5	5350745.7	Outcrop	Laminated wacke-siltstone	–	Qz	u	–	Bourgault and Boudrias (2013)

(continued on next page)

Table 1 (*continued*)

LLCFZ Segment	Sample	Deposit/Showing	UTM coordinates		Mine level/Drill hole, z (m)	Host rock	Vein thickness (cm)	Vein mineralogy	Vein type	Structural control	Ref.
			Easting	Northing							
	ALEX18	Alexandria	223855.7	5348411.7	Outcrop	Greywacke	–	Qz-Cb	u	–	Bourgault and Boudrias (2013)
Rouyn	AST1	Astoria	200243.1	5345759.1	Outcrop	Ultramafic rocks	>50	Qz-Cb	s	shear zone	Chapon (2017)
	AST2		200243.1	5345759.1	Outcrop	Ultramafic-conglo. contact	>50	Qz	e	shear zone	Chapon (2017)
	GAMB	Lac Gamble	198512.9	5345767.0	Outcrop	Ultramafic rocks	–	Qz	s	In CLLFZ	Chapon (2017)
	CIN1	Cinderella	197103.3	5346157.7	08-Cl-467, 366	Carbonate schist	250[a]	Qz-Tur	s	–	Laporte (2016)
	CIN2		197103.3	5346157.7	08-Cl-467, 367	Carbonate schist	1	Qz-Tur	s	–	Laporte (2016)
	AUG1	Augmitto	196060.2	5345867.6	Outcrop	Ultramafic rocks	<1	Qz	s	–	Laporte (2016)
	AUG2		196060.2	5345867.6	Outcrop	Ultramafic rocks	3	Qz-Tur-Cb	s	–	Laporte (2016)
	DURB37	Durbar	196012.6	5346317.0	Outcrop	Andesite	–	Qz-Cb	s	–	Tremblay (2007)
	SIL1	Silidor	197264.6	5352466.6	Mine, unknown depth	Trondhjemite	7	Qz-Cb	u	–	Carrier et al. (2000)
	SIL2		197264.6	5352466.6	Mine, unknown depth	Trondhjemite	1.5	Qz-Cb	u	–	Carrier et al. (2000)
Kirkland Lake	KL4	Skead MacGregor	145075.2	5339342.6	SM17-19, 81	Greywacke	20[a]	Qz-Ank	u	shear bands	Clarke (2016)
	KLQ	McBean	141683.0	5341948.2	Outcrop	Conglo.	–	Qz	s	highly deformed	Ispolatov et al. (2008), Hunt and Rubingh (2018)
	KL7	Munro (CanadianKirkland)	136015.2	5342477.4	MU14-89, 310	Ultramafic volcanics	1.5	Qz-Ank	u	–	Ploeger (2015)
	KL8		136015.2	5342477.4	MU14-89, 310	Ultramafic volcanics	~82.5[a]	Qz-Ank	u	–	Ploeger (2015)
	KL6	Amalgamated Kirkland	124109.3	5342701.9	AKC17-127, 969	Tuff	9.5[a]	Qz-Ank	u	mod. shear	Stevenson et al. (1995), Masson (2017)

Abbreviations: Ank = ankerite; Apy = arsenopyrite; Bt = biotite; Cal = calcite; Cb = carbonates; Ccp = chalcopyrite; Chl = chlorite; Ep = epidote; Fuc = fuchsite; Hem = hematite; Po = pyrrhotite; Py = pyrite; Qz = quartz; Ser = sericite; Tlc = talc; Tur = tourmaline; Ms = muscovite; conglo. = conglomerate; Intrusive PB= Intrusive polygenic breccia; mod. = moderate. Vein type: e = extension; s = shear; u = unknown.

[a] apparent thickness in drill hole.

piezometer equations. This kind of distribution is common for dynamically recrystallized grains in 2D and 3D, from experimentally and naturally deformed samples (Lopez-Sanchez and Llana-Fúnez, 2016). The standard deviation of the geometric mean was calculated using a function designed by Cotton (2006). As proposed by Limpert et al. (2001), confidence intervals for the geometric mean are multiplicative of the standard deviation and are noted × /(times/divide). The 2σ confidence interval (95.5%) was calculated to account for the grain size variation, to keep consistency with the minimum of 427 grain measurement for 2σ confidence. No stereological correction for conversion of 2D to 3D grain size (see Higgins, 2000, 2006) was applied on the measurements, following the recommendations for the application of the calibrated piezometer of Cross et al. (2017). The piezometer equation for geometric mean of Cross et al. (2017), which was used to calculate the flow stress, is written as follows, where D is the recrystallized grain size (μm), and σ the flow stress (MPa):

$$D = 10^{3.93\pm0.49} \times \sigma^{-1.50\pm0.25}$$

For samples displaying a bimodal grain size distribution in the logarithmic grain size histograms during the post-processing, two grain orientation maps were performed on different areas of each sample to verify that the bimodal distribution was not a local effect, and to ensure a sufficient statistical representation of each population. The bimodal distribution implies that there are probably two populations of recrystallized grains in the sample. The two populations were separated graphically by plotting the logarithm of the recrystallized grain size values and visually selecting the lower bound of the best separating histogram bin.

4. Results

4.1. Quartz microstructures

The studied samples were classified into five types according to quartz microstructures based on the deformation of porphyroclasts, the size and shape of subgrains and recrystallized grains, and the dominant DRX mechanism(s). The recrystallized grain size distribution was also used for samples that were analyzed with EBSD. The five textural types

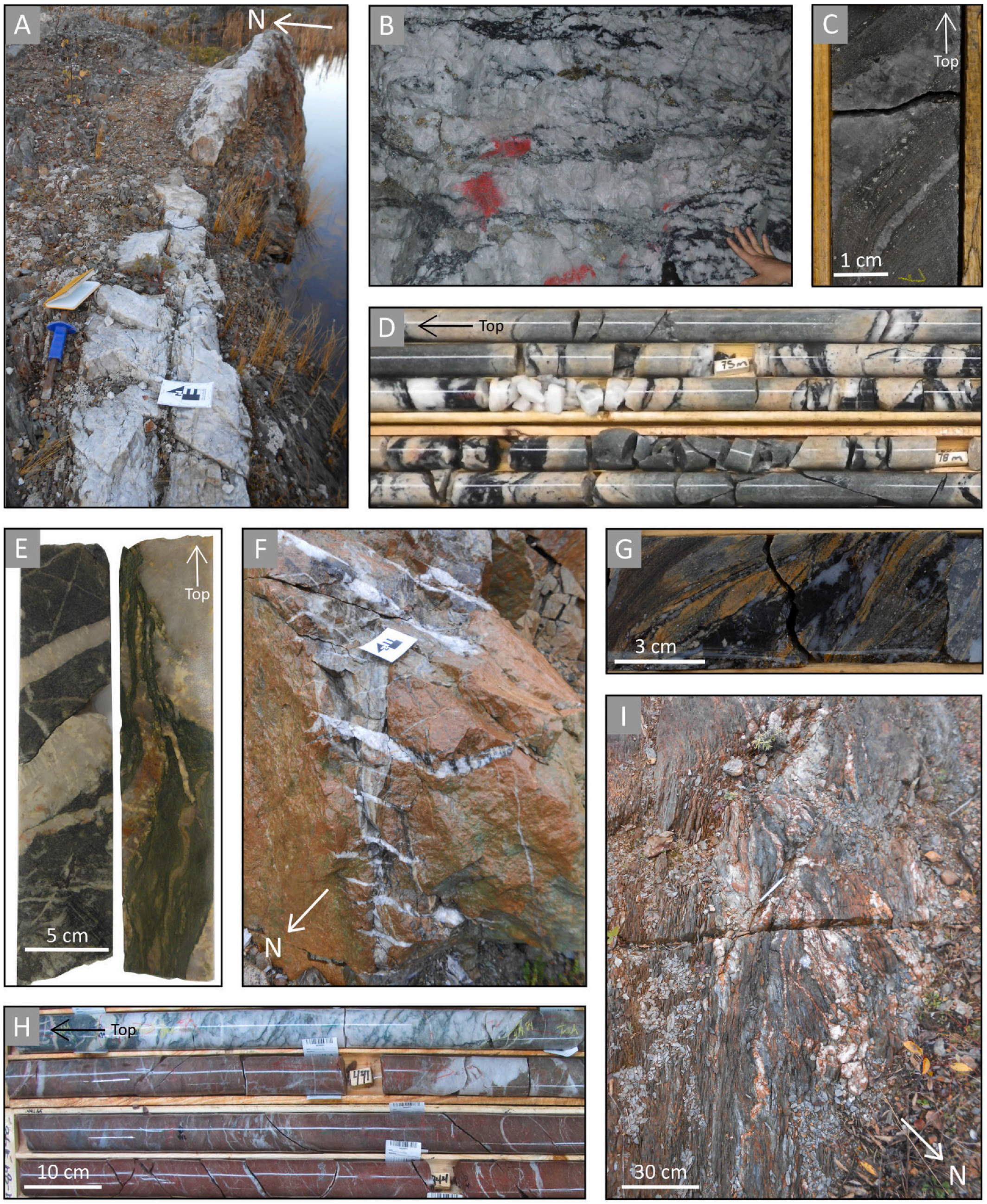

Fig. 2. Field and sample photographs. A. Dubuisson outcrop in Val-d'Or. B. Beaufor underground mine, gallery wall. C. Nordeau drill hole PG-06-07, ~460 m (mineralization). D. Goldex drill hole 65–031, ~74–80 m (sample GOLD1). E. Munro drill hole MU14-89, 438 m (sample KL7, left) and Amalgamated Kirkland drill hole AKC17-127, 1003 m (sample KL6, right). F. Augmitto outcrop near Rouy-Noranda (samples AUG1 and AUG2). G. Orenada zone 2, drill hole OAX-07-6, 414 m. H. Munro drill hole MU14-89, 437.4–448.9 m (sample KL8). I. McBean outcrop near Kirkland Lake. See Fig. 1 for sample localities. (For interpretation of the references to colour in this figure legend, the reader is referred to the Web version of this article.)

are described in the following sections and a summary is presented in Table 2. Only one sample (KL7) was not recrystallized, and exhibits preserved elongated quartz grains oriented perpendicular to vein walls, and stretched quartz grains with irregular borders, typical of syntaxial quartz growth as a result of the crack-and-seal process (Ramsay and Huber, 1983; Bons et al., 2012). Four samples were recrystallized statically (Table 2) and are described at the end of this section.

4.1.1. Type 1 microstructures

Type 1 microstructures are characterized by large porphyroclasts (few millimetres to 1 cm) and relicts of undeformed hydrothermal quartz (Fig. 4A). Porphyroclasts are elongated and of irregular shape, with a mean aspect ratio of 2. They display patchy and undulose extinction (20–50% of grains), extinction bands, and have finely bulging boundaries. Bulges of 5–26 μm and small recrystallized grains of 20 μm in average are localized at porphyroclast boundaries and along conjugate sets of shear bands and internal fractures in porphyroclasts, which typify type 1 microstructures (Fig. 5A). Intragranular fractures in porphyroclasts generally form parallel sets that locally crosscut a secondary fracture set in a different direction, and vary in orientation from one porphyroclast to the other (Fig. 5A). As suggested by Stipp et al. (2002a), this indicates that fracture orientation is probably controlled by the crystal lattice of each porphyroclast, and the presence of two fracture sets with different orientations indicates several generations of fractures (Vollbrecht et al., 1999). The fractures are commonly healed intragranular microcracks underlined by the alignment of fluid inclusions in

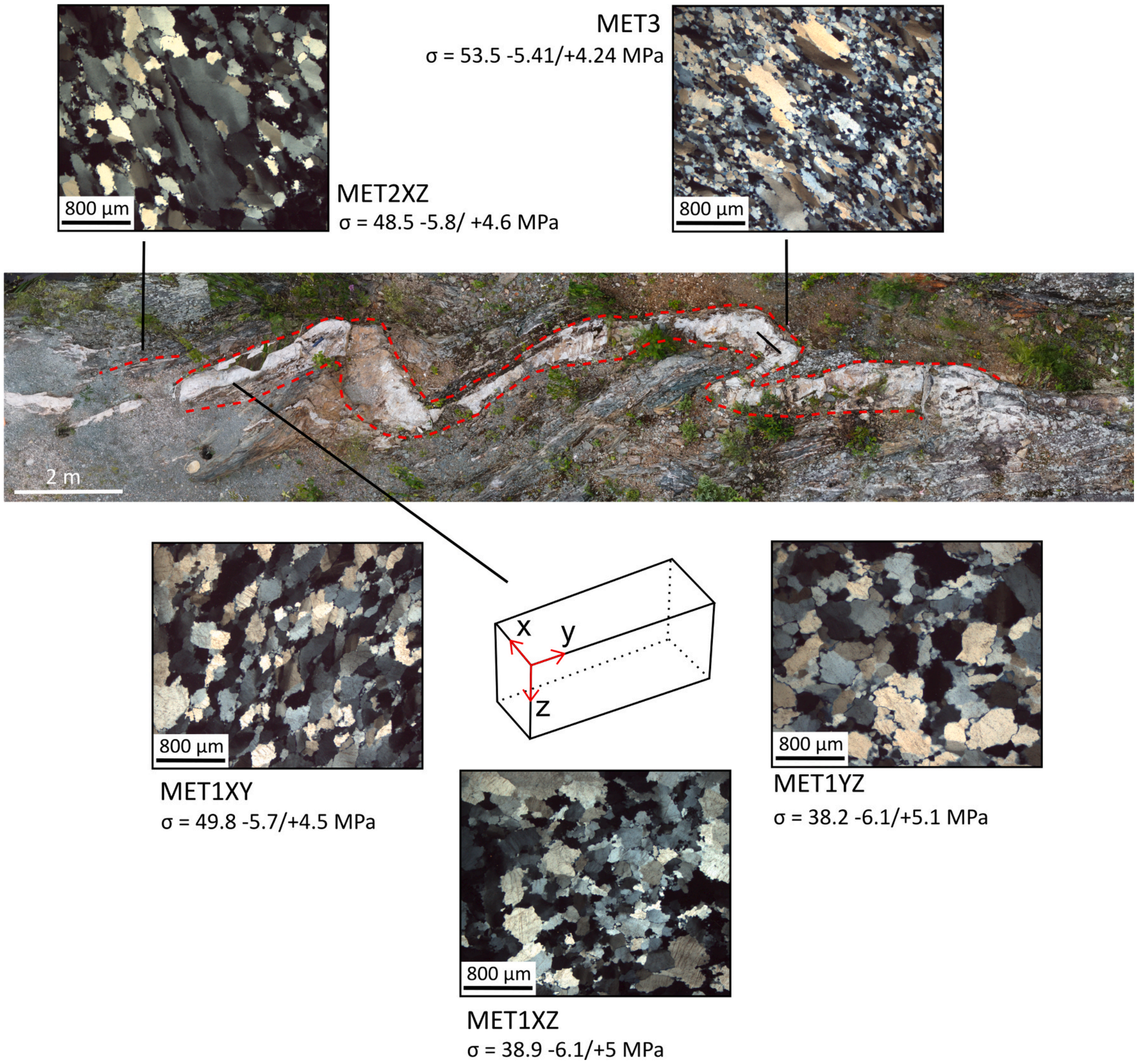

Fig. 3. Aerial drone photograph of the Dubuisson outcrop, with location of samples from this study and their respective orientation within the vein. The YZ plane represent the vertical in the vein orientation and the XY plane the horizontal surface. The photomicrograph for each sample shows its microstructures, and the flow stress calculated for each is indicated with the confidence interval below it.

most samples. Porphyroclasts generally show a high degree of internal deformation. Some samples display polygonal recrystallized grains that are larger than subgrains, and have straight or rounded boundaries, with an average grain size of 47 μm and a maximum of 100 μm (e.g., samples DURB37, KLQ). In some cases, porphyroclasts are subdivided into smaller ones (e.g., samples KLQ, KL6), and subgrains and recrystallized grains form clusters within porphyroclasts (e.g., some parts of sample KLQ). The proportion of recrystallized grains is low compared to the one of porphyroclasts. The overall characteristics of this microstructural type indicate recrystallization by BLG (Table 2).

The recrystallized grain size follows a log-normal distribution, which shows a very narrow base centered around the peak when plotted on a logarithmic scale, similarly to a narrow Gaussian distribution (Fig. 4A). The distribution is skewed towards the lower grain size values and slender curved for all the EBSD maps performed on samples from this type. The base of the distribution appears to widen when recrystallized grains are larger (e.g., samples DURB37, KLQ).

4.1.2. *Type 2 microstructures*

Type 2 quartz microstructures are characterized by a core-and-mantle texture, in which porphyroclasts have serrated but blurred boundaries from which polygonal subgrains and recrystallized grains detach progressively (Fig. 4B). The porphyroclasts generally display a uniform size and are elongated (aspect ratio of 1.4–3.6), with a long axis between 400 μm and 1 mm in average. They typically display a sweeping undulose extinction, as well as extinction bands (Fig. 5B). Porphyroclasts are either devoid of any subgrains or show a subgrain mosaic similar to the one of the surrounding subgrains and recrystallized grains. Preferential stretching of porphyroclasts in MET3 occurs at about 30° from the vertical, thus almost parallel to the fold axis. In sample AUG1, the porphyroclasts form ribbon grains similar to those found in mylonites (Fig. 5B, e g., Stipp et al., 2002a). The average size of recrystallized grains is similar to the one of subgrains and varies between 18.3 μm and 67.5 μm. The proportion of recrystallized grains varies from 5 to 20%. Sharp microstylolites are observed in OREN58 perpendicular to the vein margins.

Type 2 microstructures are typical of the transition between BLG and SGR (Table 2). The proportion of microstructures typical of SGR varies between samples and it is generally detected by the formation of straight porphyroclast boundaries, of recrystallized grains within porphyroclasts, and of a more heterogeneous grain size distribution than BLG. Samples from this type analyzed with EBSD display a Gaussian distribution either centered or negatively skewed towards the largest grain sizes (Fig. 4B).

Table 2
Microstructural type and associated recrystallization mechanism(s) for all studied samples.

LLCFZ segment	N° thin section	Deposit/ showing	Dominant DRX mecha.	Secondary DRX mecha.	Micro. Type
Val-d'Or	NORD40	Nordeau	GBM		5
	AKA54	Akasaba	–		St
	OREN58	Orenada zone 2	BLG/SGR		2
	BEAU10	Beaufor	–		St
	HERB73	Lac Herbin	–		St
	DUB16	Dubuisson	BLG/SGR		2
	DUB17		SGR-GBM		4
	MET1XY		SGR-GBM		4
	MET1XZ		SGR-GBM		4
	MET1YZ		SGR-GBM		4
	MET2XZ		SGR-GBM		4
	MET2YZ		SGR-GBM		4
	MET3		BLG/SGR		2
	GOLD2-1	Goldex	SGR	BLG	3
	GOLD2-2		SGR	BLG	3
	GOLD1		SGR		3
	GOLD3-1		GBM		5
Malartic	NORL46	Norlartic	–		St
	MCAD82	Maritime-Cadillac	SGR-GBM		4
	MCAD4		SGR	BLG	3
	MCAD6		SGR-GBM		4
	MCAD2		GBM		5
Joannes	LAPA75	Lapa	SGR-GBM		4
	OBR66	O'Brien	SGR-GBM		4
	OBR67		BLG/SGR		2
	CALD48	Calder Bousquet	SGR	BLG	3
	ZOE19	Zoé	SGR-GBM		4
	ALEX18	Alexandria	SGR		3
Rouyn	AST1XZ	Astoria	BLG		1
	AST2XY		SGR	BLG	3
	GAMB	Lac Gamble	SGR	BLG	3
	CIN1	Cinderella	SGR	BLG	3
	CIN2		SGR	BLG	3
	AUG1	Augmitto	BLG/SGR		2
	AUG2		BLG		1
	DURB37	Durbar	BLG		1
	SIL1	Silidor	SGR		3
	SIL2		BLG/SGR		2
Kirkland Lake	KL4	Skead MacGregor	SGR	BLG	3
	KLQ	McBean	BLG		1
	KL7	Munro	–		–
	KL8		BLG		1
	KL6	Amalgamated Kirkland	BLG		1

Abbreviations: BLG = bulging recrystallization; BLG/SGR = transition from BLG to SGR (core-and -mantle texture); DRX = dynamic recrystallization; mecha. = mechanism; micro. = microstructural; GBM = grain boundary migration recrystallization; SGR = subgrain rotation recrystallization; SGR-GBM = coexistance of both SGR and GBM, St = static recrystallization.

4.1.3. Type 3 microstructures

The type 3 microstructures are the most common but also the most heterogeneous (Fig. 4C, Table 2). Samples of this type exhibit porphyroclasts with a highly variable size, ranging from a few hundred μm up to 14 mm, and with an aspect ratio of 1.5–3 (Fig. 5C). These porphyroclasts display undulose extinction, local patchy extinction, and extinction bands. Porphyroclasts in a single sample display a very heterogeneous texture. Some show little indication of internal deformation, whereas others show internal deformation lamellae and local shear bands marked by bulges that resemble those found in the type 1 microstructures. Porphyroclast boundaries are highly serrated and rarely bulging. Both subgrains and recrystallized grains are polygonal, they range from 10 to 48 μm large, and are developed within, or at borders of porphyroclasts. They locally form along preferential planes or as clusters within porphyroclasts (Fig. 5C). In addition, a second group of irregular subgrains, averaging 200–300 μm in size, is found in some samples (GAMB, AST2). Those are similar to type 4 microstructures, which could indicate overlapping of different microstructural types. The sample from the Calder-Bousquet deposit is the only one that exhibits a preferential orientation of elongated subgrains and porphyroclasts (Fig. 5D). The proportion of recrystallized grains compared to the one of porphyroclasts varies greatly between samples and reaches up to ~40% of the surface of a thin section (e.g., the EBSD map of Fig. 4C).

Type 3 microstructures are dominated by SGR, and BLG to a lesser extent (Table 2). Almost all samples exhibit two populations of recrystallized grains. This distinctive feature is confirmed by the grain size statistics extracted from the EBSD data, which show a bimodal distribution of the log-transformed recrystallized grain size for four samples from this group (CIN1, MCAD4, GOLD2-2, ALEX18; histogram of Fig. 5C). However, the log-transformed data show a normal distribution for the samples from the Goldex (GOLD1), Silidor (SIL1), and Astoria deposits (AST2). These samples are mostly dominated by SGR in microstructural observations.

4.1.4. Type 4 microstructures

Specific features of the type 4 microstructures are the homogeneous size distribution of the porphyroclasts and recrystallized grains, and the irregular shape and boundaries of subgrains and recrystallized grains (Fig. 4D). Some samples exhibit few remnants of large porphyroclasts (maximum 4 mm in MET2) that contain a high proportion of subgrains, giving them a patchy extinction. However, the difference in size between porphyroclasts and recrystallized grains is much lower than in the other textural types (Fig. 4D). Porphyroclasts are 750 μm in average and are less than 2 mm long, with an aspect ratio of 1.2–1.8. They display frequent undulose extinction that occurs in about 20% of the grains and up to 40% in the samples from the Maritime-Cadillac deposit, and few extinction bands. Porphyroclasts have serrated to irregular boundaries that extend outwards into cloud-like boundaries. Samples from the Maritime-Cadillac deposit are distinguished by porphyroclasts with bulging boundaries and a high heterogeneity of quartz microstructures. Deformation lamellae are abundant in type 4 microstructures, especially in samples from the Dubuisson property and Lapa deposit (Fig. 4D). Subgrains are either polygonal and 30–50 μm wide, or they divide larger porphyroclasts into irregular 130–392 μm subgrains. The polygonal subgrains are separated from porphyroclast boundaries. Most recrystallized grains are similar in shape and size to the irregularly shaped subgrains and reach up to 600 μm lengthwise. The recrystallized grains are only distinguished from porphyroclasts by the absence of internal deformation. Polygonal recrystallized grains are uncommon (e.g., sample ZOE19). The proportion of recrystallized grains is variable between samples, but samples that are fully recrystallized tend to form an equigranular grain aggregate (Fig. 4D). Solid and fluid inclusions are common, especially in the samples from the Dubuisson property (MET1, MET2) and Zoé showing, where they form inclusion bands that are either parallel to each other or at a 60° angle. These bands are generally restricted to a single grain or subgrain. The inclusions account for up to 5–10% of porphyroclast surfaces.

Type 4 microstructures probably originate from GBM and SGR recrystallization (Table 2), as there is a tendency to have larger recrystallized grains than in the other microstructural types. The recrystallized grain size extracted from the EBSD maps have a broad distribution that is positively skewed, except for sample LAPA75, which shows a negatively skewed distribution (Fig. 4D).

4.1.5. Type 5 microstructures

Samples from type 5 microstructures are characterized by a low proportion of porphyroclasts, with irregular boundaries and undulose extinction (Fig. 4E). The porphyroclasts are of variable size and shape, generally a few mm in diameter and with an aspect ratio comprised between 1.5 and 3. Subgrains occur at porphyroclast boundaries or less frequently within porphyroclasts and are locally abundant. The size of

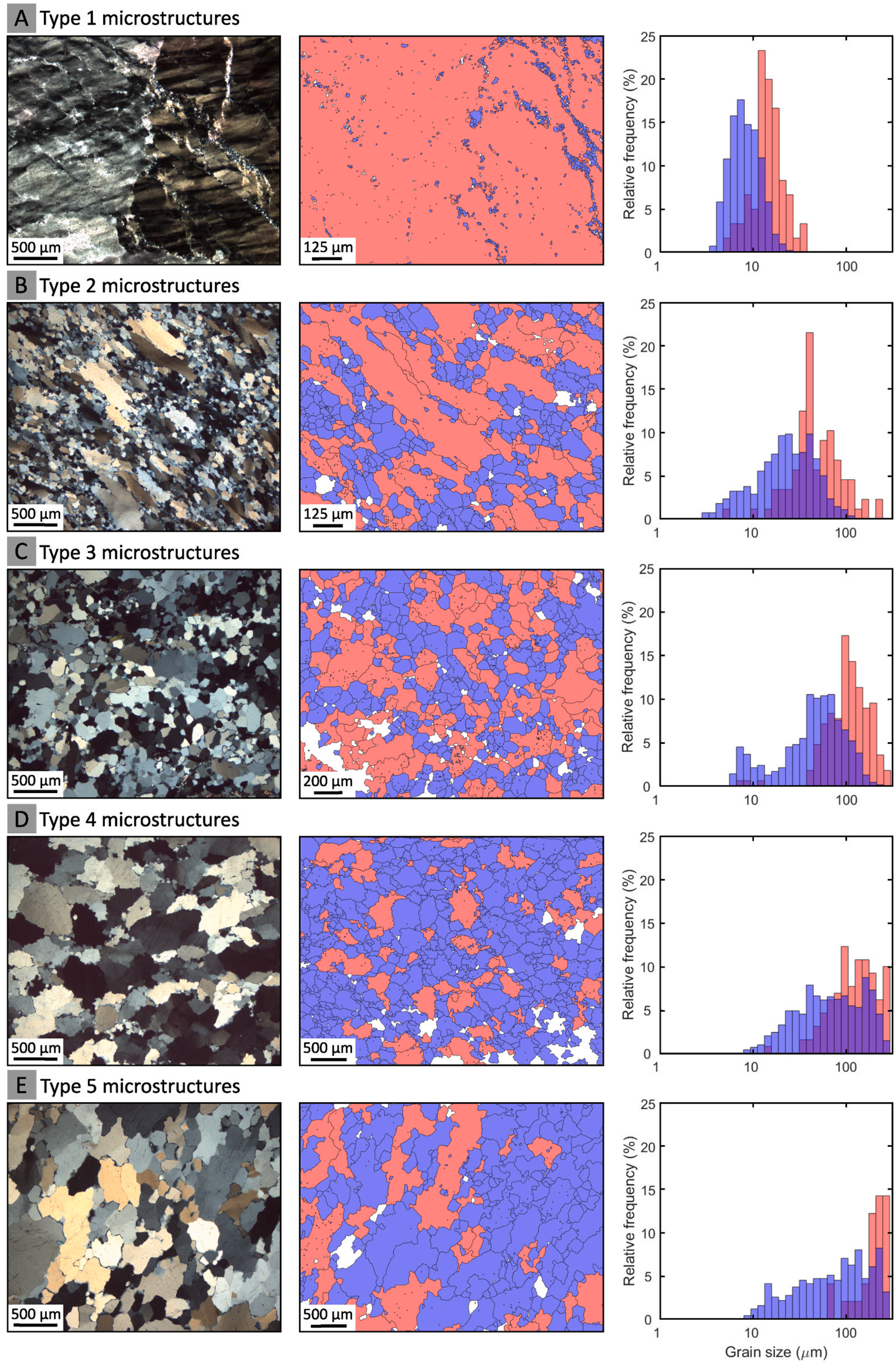

Fig. 4. Types of dynamic recrystallization microstructures found in samples from this study. Comparison between microstructures observed under cross-polarized light, final EBSD map with relict (red) and recrystallized (blue) grains, and respective distribution of recrystallized grain size extracted from the EBSD data post-processing. The grain size distribution histograms are drawn using the log-transformed data and the relative frequencies of relict and recrystallized grains (see Cross et al., 2017). White patches are areas of non-indexed pixels. Note that the EBSD maps and microphotographs do not correspond exactly to the same area. A. Types 1 microstructures example with a sample from the Munro showing (KL8). B. Type 2 microstructures example with a sample from the Dubuisson property from the hinge of a fold (MET3). C. Type 3 microstructures example with a sample from the Alexandria showing (ALEX18). Note the bimodal distribution of recrystallized grain sizes. D. Type 4 microstructures example with a sample from the Lapa deposit (LAPA75). E. Type 5 microstructures example with a sample from the Goldex deposit (GOLD3, 1493 m). See Fig. 1 for sample localities. (For interpretation of the references to colour in this figure legend, the reader is referred to the Web version of this article.)

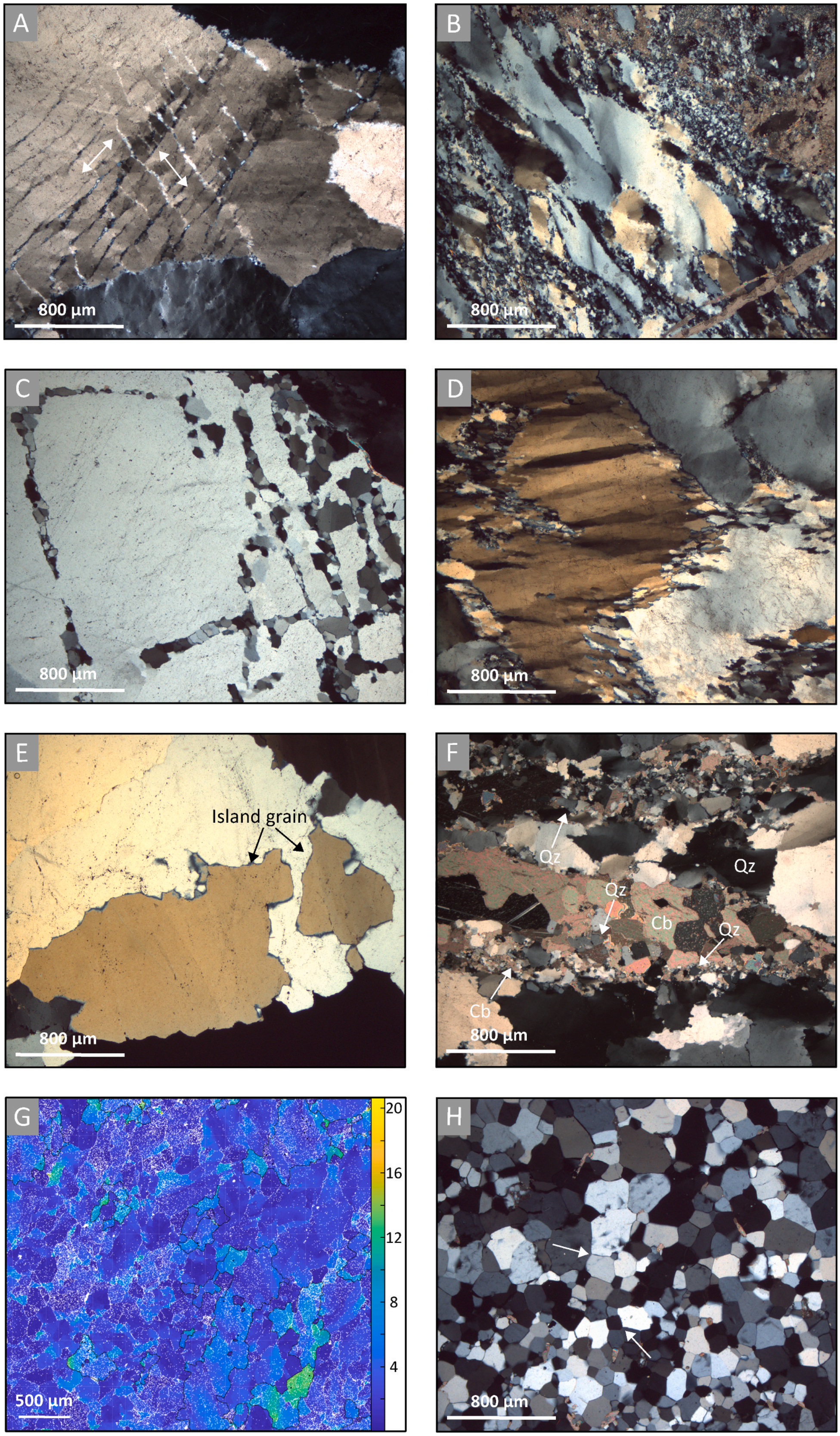

(caption on next page)

Fig. 5. Specific microstructures found in samples from this study. Photomicrographs taken under cross-polarized light. A. Orthogonal fractures in porphyroclast of sample KL6 from the Munro deposit. The two directions are indicated by the double arrows. B. Ribbon porphyroclasts with core-and-mantle texture in sample AUG1 from the Augmitto showing. Recrystallization mainly occurs at porphyroclast borders, and porphyroclasts exhibit sweeping undulose extinction. C. Orthogonal bands of recrystallization in a porphyroclast of sample SIL1 from the Silidor deposit. D. Elongation of porphyroclast and subgrains in sample CALD48 from the Calder-Bousquet showing. E. Example of an island grain in sample NORD40 from the Nordeau deposit. This texture is typical of grain boundary migration and occurs when one grain is separated in two or more by the preferential development of another grain. F. Grain size reduction of quartz in areas of high carbonate concentration in Maritime-Cadillac sample MCAD2. G. Misorientation map extracted from EBSD analysis of sample GOLD3 from the Goldex deposit. H. Typical layout of quartz grains recrystallized by static recrystallization, with triple grain junction (arrows) and equigranular grain aggregate, in sample NORL46 from the Norlartic deposit. See Fig. 1 for sample localities. (For interpretation of the references to colour in this figure legend, the reader is referred to the Web version of this article.)

subgrains and recrystallized grains is highly variable, ranging from 50 μm to 500 μm. Polygonal subgrains and recrystallized grains of about 20 μm–40 μm in size are present locally. The amoeboid shape of subgrains and recrystallized grains with straight and irregular boundaries, as well as the presence of island grains (Fig. 5E), are all indicative of GBM.

Fluid inclusions vary greatly in proportion and form trails within the largest porphyroclasts (Nordeau deposit) or are aligned along grain boundaries (Goldex deposit). In the sample from the Nordeau deposit (450 m depth), numerous quartz grains contain fluid inclusion bands despite the dominance of GBM, which suggests that this sample recrystallized under conditions close to the SGR/GBM transition, similarly to what is presented in Stipp et al. (2002a). The deepest sample from Maritime-Cadillac (MCAD2, 453 m) exhibits type 5 microstructures, but also displays a heterogeneous distribution of microstructures, and a high proportion of serrated grain boundaries and subgrains. However, the smaller grain size of quartz in areas where carbonates are abundant may indicate a possible grain size reduction due to mineralogical heterogeneity (Fig. 5F). This effect and the pinning of grain boundaries are microstructures typical of GBM in presence of second phase particles (e.g., Stipp et al., 2002a; Humphreys and Hatherly, 2004).

Type 5 microstructures are dominated by GBM recrystallization

Table 3
EBSD analysis results and calculated flow stress (σ). The recrystallized grain size (RX) geometric mean is indicated with its corresponding geometric standard deviation, expressed in × /(times/divide). See the Analytical methods for detailed explanation.

Sample	Deposit	σ (MPa)			Step size (μm)	Area (mm^2)	# of maps	Indexing Rate (%)[b]	Total No. of Grains	No. of Relict Grains	No. of RX Grains	RX d geo. mean (μm)	Geo. Std (2σ)
			min[a]	max[a]									
OREN58	Orenada 2	51.3	45.7	55.6	1.78	3.05	2	88.5	1919	156	1763	23.2	4.8
MET1XY	Dubuisson	49.8	44.1	54.3	1.60–3.21	6.17	2	88.8	641	94	547	24.2	6.3
MET1XZ		38.9	32.8	43.9	3.21	4.94	1	91.6	527	36	491	35.1	6.3
MET1YZ		38.2	32.1	43.3	2.29–3.21	7.45	2	92.5	696	82	614	36.0	6.9
MET2XZ		48.5	42.7	53.1	3.21	4.94	1	84.8	656	47	609	25.2	4.4
MET3		53.5	48.1	57.7	1.60	1.37	2	81.4	647	88	559	21.8	4.4
GOLD2-2[c]	Goldex	49.3	43.5	53.8	2.29	2.52	2	87.8	524	78	446	24.6	5.7
GOLD1		39.8	33.7	44.8	2.29	7.55	3	77.8	578	71	507	33.9	4.5
GOLD3		21.2	15.8	26.1	5.34	35.1	3	91.2	560	49	511	87.3	7.6
MCAD4[c]	Maritime -Cadillac	51.5	45.9	55.9	1.60	3.70	3	86.6	778	115	663	23.0	6.2
MCAD82		43.4	37.4	48.2	2.29	5.03	2	86.3	300	27	273	29.8	5.6
MCAD2		33.3	27.2	38.4	2.67–9.16	23.6	3	74.9	382	45	337	44.4	6.5
LAPA75	Lapa	24.1	18.5	29.2	4.01–5.34	21.4	2	87.3	1174	130	1044	71.7	5.5
ALEX18[c]	Alexandria	34.3	28.2	39.5	2.67	6.86	2	85.6	882	168	714	42.3	5.2
AST1	Astoria	74.5	71.5	76.7	1.46	1.02	1	83.3	539	102	437	13.2	3.1
AST2		46.1	40.2	50.8	2.29	2.52	1	77.9	692	102	590	27.2	5.3
CIN1[c]	Cinderella	52.8	47.4	57.1	1.60–1.78	3.98	3	85.4	954	122	832	22.2	3.7
DURB37	Durbar	56.9	51.7	60.8	2.67	3.43	1	93.3	2585	358	2227	19.8	3.6
SIL1	Silidor	31.6	25.6	36.8	3.21	4.94	1	87.0	642	68	574	47.9	4.8
SIL2		37.6	31.5	42.6	3.21	9.87	2	84.0	1937	297	1640	37.0	3.1
KLQ	McBean	68.9	65.2	71.8	1.60	2.47	2	84.4	1520	127	1393	14.9	3.8
KL8	Munro	103	106	102	1.60	1.23	1	85.9	865	60	805	8.10	2.1
KL6	Amalg.	80.0	77.9	81.5	1.46	1.02	1	67.5	1448	130	1318	11.9	3.0

Abbreviations: d = grain size diameter; geo. = geometric; RX = recrystallized; Std = standard deviation.
[a] Lower and upper bounds for piezometer are calculated from the equation uncertainty.
[b] For samples with multiple maps, the arithmetic mean of the respective indexing rates of each map was calculated.
[c] Bimodal distribution, calculated grain size and flow stress are not representative of the sample.

(Table 2). The EBSD maps performed on one sample representative of type 5 microstructures (GOLD3) show that the internal misorientation is relatively small for most grains (Mis2Mean < 6, Fig. 4G), but porphyroclasts are still distinguished by their higher level of internal misorientation (Mis2Mean > 6, Fig. 4G). The recrystallized grain size varies between 10 and 500 μm, with a very broad distribution (Fig. 4E). Such a distribution is expected because GBM induces a wider range of recrystallized grain size than the other DRX mechanisms (e.g., Stipp et al., 2002a). A concentration of grains below 50 μm is due to the presence of relatively small polygonal recrystallized grains (Fig. 4E).

4.1.6. *Static recrystallization microstructures*

Four samples from this study exhibit static recrystallization (Table 2), and for this reason they were not analyzed by EBSD. These samples show a very low proportion of porphyroclasts with a slight undulose extinction. Recrystallized grains are commonly equant, polygonal or diamond shaped, and average 170 μm in size (Fig. 5H). Their boundaries are straight and clean, and they form 120° triple junctions typical of static grain growth (Fig. 5H). Some samples show pyrite crystals with pressure fringes composed of fibrous quartz. Grain boundaries are clearly visible in plane polarized light, and recrystallized grains are generally inclusion-free.

4.2. *EBSD and paleopiezometry*

The EBSD data post-processing allowed the calculation of the grain size geometric mean, the geometric standard deviation, and the flow stress (Table 3). Only two samples (MCAD2 and MCAD82) did not reach the grain count threshold value of 427 grains to be used in piezometer equations with sufficient certainty (Lopez-Sanchez, 2020). As mentioned in the previous section, four samples belonging to the type 3 microstructures display a bimodal distribution in the grain size histograms. For these samples, two grain size populations were split to calculate independently the mean grain size and flow stress for each population (Table 4).

In the samples from the Kirkland Lake area (Fig. 1), the recrystallized quartz grains range from 8.10 × /2.1 to 14.9 × /3.8 μm, and the calculated flow stress is higher than in all of the other samples analyzed in this study, ranging from 68.9 + 2.8/-3.8 to 103 + 3/-2 MPa. In the Rouyn-Noranda area (Fig. 1), the recrystallized grain size ranges from 13.2 × /3.1 μm at the Astoria deposit, to 47.9 × /4.8 μm at the Silidor deposit, and the corresponding flow stress from 74.5 + 2.2/-3.0 to 31.6 + 5.2/-6.0 MPa. The samples from the Joannes segment (Fig.1) yield the largest recrystallized grain size mean and the lowest flow stress values, for both surface (28.2 + 5.1/-5.9 MPa; Alexandria showing, Table 4) and underground samples (24.1 + 5/-5.6 MPa; Lapa deposit) except for the deepest sample from the Goldex deposit. The samples from the Maritime-Cadillac deposit, at the eastern extremity of the Joannes segment (Fig. 1), yield a similar recrystallized grain size mean and flow stress to those of the Goldex deposit on the Malartic segment, as well as those on the Val-d'Or segment. These samples have recrystallized quartz grains that range from 21.8 × /4.4 to 87.3 × /7.6 μm, which corresponds to flow stress values of 21.2 + 4.9/-5.4 to 53.5 + 4.2/-5.4 MPa; with a mean of 43.4 MPa (Tables 3 and 4). Samples exhibiting type 3 microstructures analyzed with EBSD are characterized by a bimodal recrystallized grain size distribution (e.g., Fig. 4C). The grain size histograms show two peaks of different intensities: the peak for the smallest grains represents less than 19% of the recrystallized grains in the three samples with more than 427 recrystallized grains, and a maximum of 43% for sample GOLD2-2 (Table 4). The second peak represents a majority of the recrystallized grains for all samples, and corresponds to larger grain sizes. A dominant population of SGR-dominated recrystallized grains giving a flow stress of 28.22 + 5.1/-5.9 to 49.9 + 4.5/-5.7 MPa (Table 4) compete with another population of smaller BLG-dominated recrystallized grains that yield flow stress values of 94.3 + 0.6/-0.4 to 153 + 17/-11 MPa (Table 4). The GOLD2-2 sample was the only one that did not reach the grain count threshold after the population split.

Table 4
Grain size and calculated flow stress for separated populations of the samples displaying a bimodal recrystallized grain size distribution.

Sample	RX grains population	σ (MPa)			No. of RX Grains	RX d geo. mean (μm)	Geo. Std (2σ)
		σ	min[a]	max[a]			
GOLD2-2	Pop 1	35.6	29.5	40.7	311	40.1	2.9
	Pop 2	104	102	107	135	8.0	1.6
MCAD4	Pop 1	42.5	36.5	47.4	564	30.7	3.7
	Pop 2	153	142	169	99	4.5	1.3
ALEX18	Pop 1	28.2	22.3	33.4	598	56.8	2.8
	Pop 2	94.3	93.9	94.9	116	9.3	1.8
CIN1	Pop 1	49.1	43.3	53.6	775	24.7	3.0
	Pop 2	140	131	152	57	5.1	1.3

[a] Lower and upper bounds for piezometer are calculated from the equation uncertainty.

4.3. *Methodological tests*

4.3.1. *Influence of folding*

Following the study of the various samples from the Dubuisson deposit (Fig. 3), the sample MET3, which comes from the hinge of a fold affecting the principal vein, exhibits a very different texture from the other samples collected on the same outcrop. It is characterized by a core-and-mantle texture (type 2, Figs. 3 and 4B), indicative of BLG-SGR transition, unlike samples MET1 and MET2, which are dominated by GBM and SGR. Porphyroclasts are of similar size compared to samples MET1 and MET2 (~1 mm in average), but are more elongated, with an aspect ratio of 1.4–3, and have highly serrated boundaries. Subgrains and recrystallized grains in MET3 are polygonal, whereas they are generally irregular in samples MET1 and MET2 (Fig. 3). The subgrains average 50 μm in size and the recrystallized grains range from 50 to 100 μm, which is significantly smaller than those of samples MET2XZ (average of 115 μm) and MET1 (ranging between 130 and 392 μm). The grain size extracted from the EBSD data is 21.8 × /4.4 μm for recrystallized grains, which is much smaller than what was inferred from optical observations only. The flow stress was calculated at 53.5 + 4.2/-5.4 MPa and is thus higher than what was documented for samples MET1 and MET2 (Table 3, Fig. 3). As such, the grain size is smaller and the calculated flow stress is much higher in the hinge than along the limbs of the vein.

4.3.2. *Influence of depth*

Samples from the Goldex and Maritime-Cadillac deposits were sampled from drill cores at different depths to determine the influence of depth on microstructures and recrystallized grain size (Table 1).

Goldex deposit: In samples from the Goldex deposit, the shallowest samples (GOLD2-1 and GOLD2-2, 261 m) exhibit type 3 microstructures, dominated by SGR (Fig. 6A and B). Porphyroclasts range from 7 mm to 14 mm (GOLD2-2) and from 2 mm to 4 mm (GOLD2-1). Their aspect ratio is 2 in average, and their boundaries are highly serrated, and locally show bulging (GOLD2-2). Porphyroclasts exhibit patchy extinction or extinction bands, deformation lamellae, and small subgrains (<10 μm) are locally found along internal deformation bands (GOLD2-2), which are similar to what is found in type 1 microstructures (Fig. 6A). Polygonal subgrains and recrystallized grains generally form along porphyroclast boundaries, although subgrains are also observed within

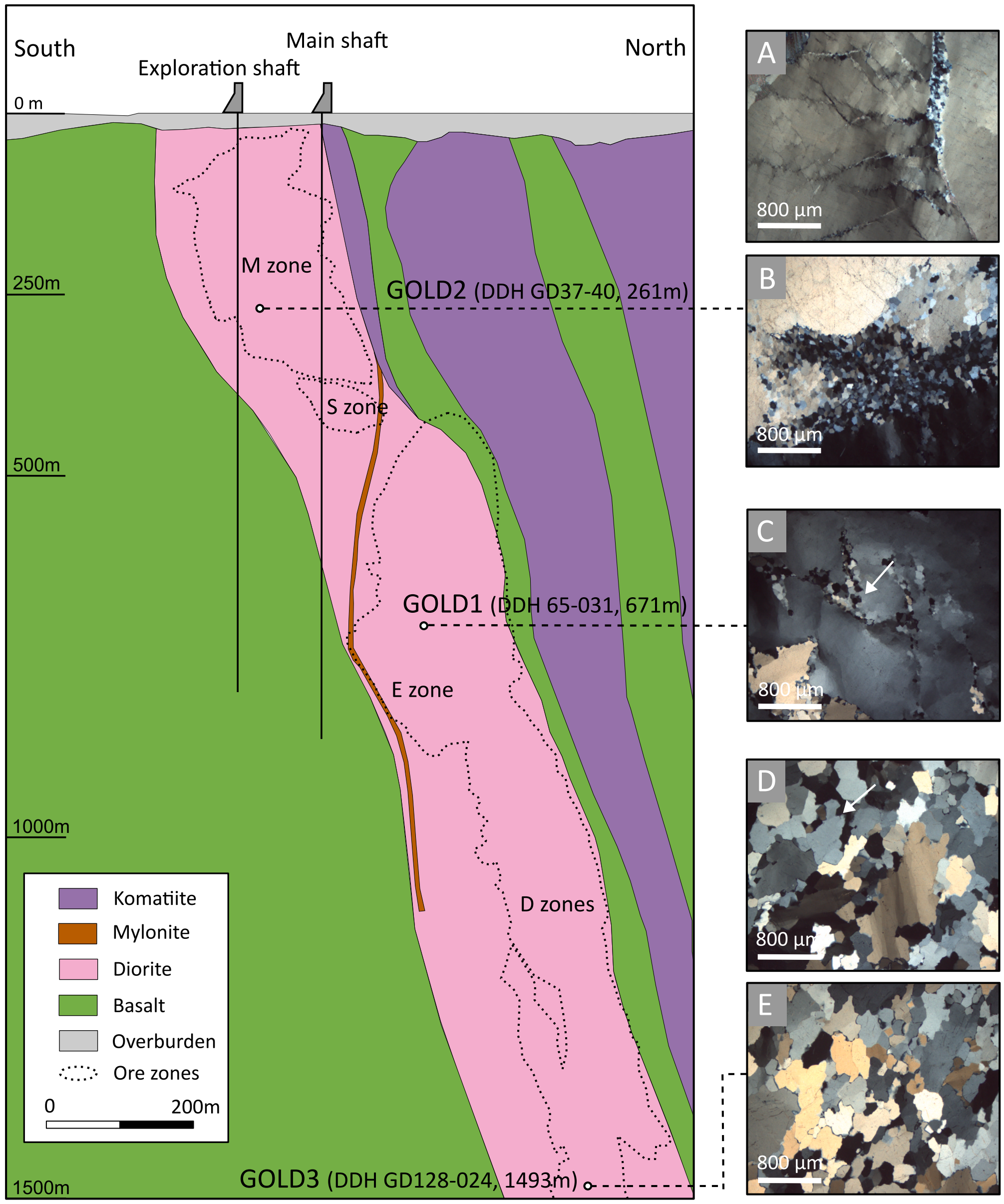

Fig. 6. Schematic cross section of the Goldex deposit with approximate location of drill hole samples respective to depth. A. Internal deformation and bulging similar to type 1 microstructure in sample GOLD2-2. B. Area of recrystallization between two porphyroclasts in sample GOLD2-2. C. Formation of subgrains within porphyroclasts in sample GOLD1. D. Two remaining porphyroclasts, which can be identified by the extinction bands, in a mostly recrystallized area of sample GOLD3. Grains and subgrains have irregular boundaries (arrow) and irregular shapes. E. Area of fully recrystallized grains by GBM in sample GOLD3. See Fig. 1 for samples locality. (For interpretation of the references to colour in this figure legend, the reader is referred to the Web version of this article.)

porphyroclasts (Fig. 6B). Subgrain size is 32 μm in average for GOLD2-1 and 41 μm for GOLD2-2. Recrystallized grains are abundant and porphyroclasts are highly deformed (Fig. 6A). The EBSD data from GOLD2-2 mapping gives a mean grain size of 24.6 × /5.7 μm for all recrystallized grains (Table 3). However, when splitting the bimodal distribution into two separate grain populations, the larger population (311 grains, <427 grains threshold) yields a geometric mean of 40.1 × /2.9 μm (Table 4).

The second sample, from 671 m depth (GOLD1), also exhibits type 3 microstructures and is dominated by SGR. This sample contains the largest porphyroclasts, that reach up to 12 mm in size, have serrated boundaries similar to those of GOLD2 samples, and contain deformation lamellae (Fig. 6C). These porphyroclasts rarely exhibit undulose extinction. Polygonal subgrains have an average grain size of 60 μm, which is larger than for GOLD2 samples, and may locally form within porphyroclasts (Fig. 6C). Recrystallized grains are of similar size and shape to subgrains, and form at porphyroclast boundaries similarly to GOLD2 samples. However, recrystallized grains are uncommon compared to GOLD2 samples. The microstructures are very similar to those of sample GOLD2-1, but the low internal deformation of porphyroclasts and the low proportion of recrystallized grains indicate that the deformation was heterogeneous compared to GOLD2 samples. The recrystallized grain size extracted from EBSD data is 33.9 × /4.5 μm, which corresponds to a flow stress of 39.8 + 5.0/-6.1 MPa. The grain size is comparable to the one obtained for the largest population of GOLD2-2 given the uncertainty (40.1 × /2.9 μm).

The deepest sample from the Goldex deposit (GOLD3, 1493 m) displays a distinct texture, belonging to type 5 microstructures, relative to the one of the three shallower samples (GOLD1, GOLD2-1 and GOLD2-2). It shows amoeboid grain aggregates, uncommon 1–2 mm long porphyroclasts, and a majority of irregular recrystallized grains that are typical of GBM recrystallization (Fig. 6D and E). Recrystallized grain size is 87.3 × /7.6 μm and the resulting flow stress is comprised between 15.8 and 26.1 MPa (21.2 + 4.9/-5.4 MPa), which is much lower than what was calculated for GOLD1 and GOLD2-2 (Tables 3 and 4).

Maritime-Cadillac deposit: In the samples from the Maritime-Cadillac deposit, the shallowest sample (MCAD4, 36 m) exhibits type 3 microstructures, with 1–4 mm porphyroclasts that have highly serrated boundaries. Porphyroclasts exhibit undulose extinction, deformation lamellae, and rare extinction bands (Fig. 7A). Their aspect ratio is comprised between 1 and 2. Polygonal subgrains and recrystallized grains are about 34 μm in average, and generally form between porphyroclasts, or less frequently within them (Fig. 7A). The recrystallized grain size extracted from EBSD data shows a bimodal distribution for this sample. Splitting of the two populations gives a mean grain size of 30.7 × /3.7 μm for the larger population (564 grains, Table 4) and 4.5 × /1.3 μm for the minor population (99 grains). The resulting flow stress is 42.5 + 4.9/-6.0 MPa for the main population of recrystallized grains.

The second sample, from 169 m depth (MCAD6), displays a texture distinct from MCAD4, which is composed of a more homogeneous equigranular aggregate belonging to type 4 microstructures (Fig. 7B). The porphyroclasts are smaller (1.4 mm in average), have an aspect ratio of 1.7 similar to MCAD4 porphyroclasts. Subgrains are less abundant compared to MCAD4. They are either large (267 μm in average) and form within porphyroclasts, or occur as bulges (24 μm in average) located at porphyroclast boundaries (Fig. 7B). Recrystallized grains have irregular shapes and sizes (146 μm in average), and reach up to 1 mm. This sample was not analyzed with EBSD because of the large proportion of carbonates, but the recrystallized grains described above that were optically recognized are generally much larger than the ones in MCAD4.

In the sample from 280 m depth (MCAD82), microstructures also belong to type 4, but porphyroclasts are commonly smaller than in the two previous samples, with an average long axis of 720 μm (Fig. 7C). The aspect ratio is about 1.5, and porphyroclast boundaries are highly serrated, similarly to sample MCAD6. Porphyroclasts generally display undulose extinction or extinction bands. Subgrains are more abundant than in sample MCAD6 (Fig. 7C). Subgrains and recrystallized grains are polygonal (30 μm in average) or irregular (400 μm in average, up to 500 μm) and are both located within porphyroclasts or at their boundaries. The recrystallized grain size is 29.8 × /5.6 μm (n = 300 grains, <427 grains threshold), which is in the same range as the recrystallized grain size of sample MCAD4 (Tables 3 and 4).

The deepest sample (MCAD2, 453 m) is likely dominated by GBM, with minor SGR recrystallization (type 5 microstructures). Porphyroclasts generally display irregular shapes with serrated or irregular boundaries (Fig. 7D). They are similar in size and shape to the ones in samples MCAD6 and MCAD82, but are generally more elongated, with an aspect ratio of up to 2.9. Few deformation lamellae and extinction bands are visible compared to the other samples from the Maritime-Cadillac deposit (Fig. 7D). Subgrains and recrystallized grains are larger than in the other samples, ranging from 400 to 800 μm. The post-processed maps from the EBSD data display a large proportion of recrystallized grains. The calculated geometric mean is 44.4 × /6.5 μm (382 grains, <427 grains threshold), giving a flow stress of 33.3 + 5.2/-6.1 MPa.

All samples from the Maritime-Cadillac deposit contain a large proportion of carbonates. Some late carbonate veinlets crosscut quartz grains, but other carbonate aggregates likely crystallized and

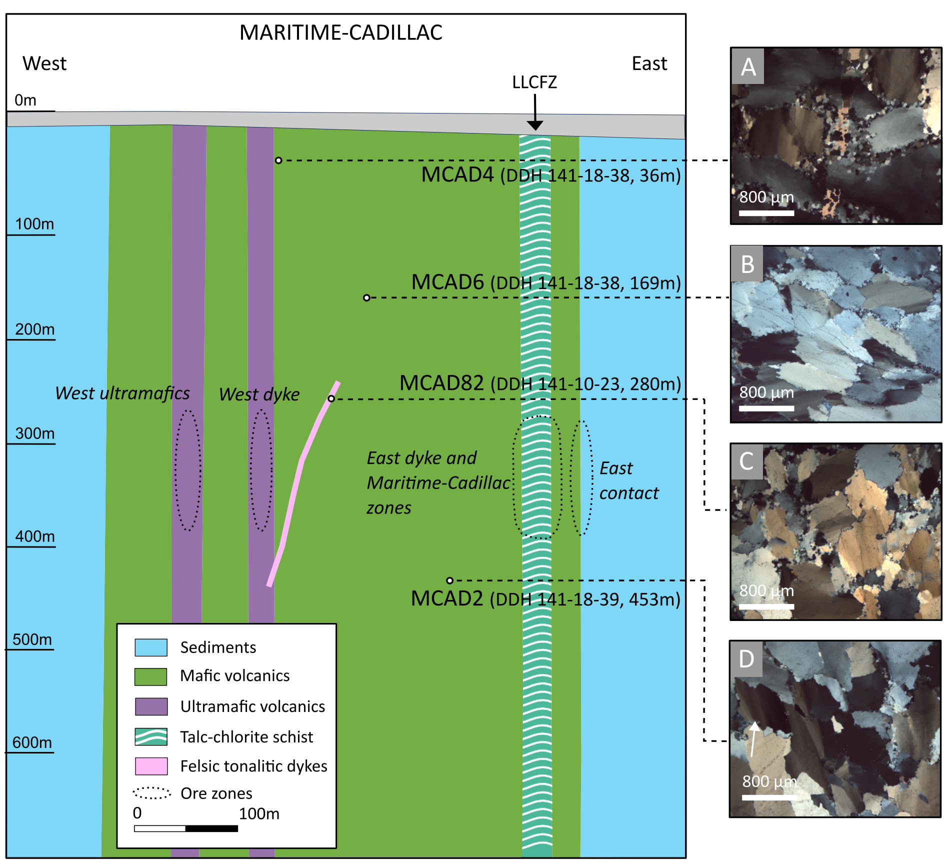

Fig. 7. Schematic cross section of the Maritime-Cadillac showing with projected location of drill hole samples respective to depth. A. Porphyroclasts exhibiting internal deformation (extinction bands), subgrains and recrystallized grains between porphyroclasts in sample MCAD4. B. Porphyroclasts with serrated boundaries and large subgrains in sample MCAD6. Note the abundance of fluid inclusions in the porphyroclasts. C. Abundant subgrains in sample MCAD82. D. Irregular elongated shape of porphyroclasts and recrystallized grains in sample MCAD2. See Fig. 1 for samples locality.

recrystallized within the quartz matrix. The smallest (30–200 μm) quartz grains and subgrains are rounded and undeformed or exhibit undulose extinction, and are generally enclosed within carbonates aggregates (Fig. 5G). The presence of carbonates in the matrix and/or of late crosscutting carbonate veinlets, may have affected quartz recrystallization processes within the veins.

Although the samples from the Goldex and Maritime-Cadillac deposits exhibit different types of microstructures or variations in the textures documented, they both demonstrate an increase in the recrystallized grain size with increasing depth. This trend is related to a transition in the dominant recrystallization mechanism, from SGR to GBM.

5. Discussion

5.1. Local microstructural and flow stress variations in quartz veins

Textural variations documented in this study suggest that the effect of folding is significant as it induces grain size reduction, a different dominant recrystallization mechanism and thus a different microstructural type in the hinge compared to the limbs or unfolded parts of the vein (sample MET3, Table 3, Fig. 3), which is similar to the results of other studies (e.g., Schmatz and Urai, 2011). Variation in microstructures and flow stress within a fold can be explained by local strain partitioning and recrystallization in the hinge (e.g., Trepmann and Stöckhert, 2009). Similarly, the presence of carbonates within quartz veins from the Maritime-Cadillac deposit was shown to affect the microstructures, and possibly the grain size (Fig. 5G). During ductile deformation, the rock rheology depends on numerous factors such as its mineral composition, grain size, fluid content, and ultimately on the

Table 5
Comparison of microstructures found in quartz from this study and selected studies on metamorphic rocks and quartz veins, for each dominant dynamic recrystallization mechanism.

		This study	Stipp et al. (2002a)	Hunter et al. (2021)	Kidder et al. (2013)	Trepmann and Seybold (2019)
	Quartz type	Hydrothermal quartz veins	Quartz veins/bands in mylonites	Quartzites	Quartzite and quartz veins	Quartz veins in metasediments
	Environment	Orogeny, SZ	Strike-slip FZ + contact aureole	Orogeny, Thrust FZ	Orogeny	Orogeny, Extensional SZ
BLG high stress-low T def.	Prcl shape	irregular, aspect ratio 1 to 4	± elongated	–	flattened	elongated
	Prcl size	pluri-cm to pluri-mm	Pluri-mm	–	ave. 500 μm	pluri-mm
	Internal def.	- extinction bands - undulose and patchy ext. - conjugate sets of shear bands	- undulose and patchy ext. - def. bands - def. lamellaes - conjugate sets of shear bands	–	- undulose ext. - rare def. lamellae	- short wavelength undulose ext. - conjugate sets of micro-shear bands - sub-basal def.lamellaes - Dauphiné twins
	Boundaries	finely serrated and bulging	finely serrated	–	serrated	sutured, fluid inclusions alignment
	Subgrains	bulges, polygonal along shear bands and at borders	bulges at triple junctions, along internal fractures locally large irregular	–	irregular, variable sizes	similar to RX grains along micro-shear zones, boundaries and cracks
	RX grains size	20–50 μm in average	5–25 μm	–	10–20 μm	<10 μm
SGR inter. stress- T def.	Prcl shape	aspect ratio 1.5 to 3	highly elongated	rounded to elliptical	unknown, overprinting	–
	Prcl size	generally pluri-mm	lengths pluri-mm	800 μm/2–3 mm	–	–
	Internal def.	- undulose and patchy ext. - frequent def. lamellaes	less frequent than BLG	–	–	–
	Boundaries	serrated, straighter	straighter than BLG	serrated	–	–
	Subgrains	25–60 μm, similar to RX grains inside and at prcl borders	same as RX grains	similar to RX grains	similar to RX grains	–
	RX grains			–	strong oblate shape	–
	RX grains size	20–40 μm in average generally at prcl borders	60–85 μm	–	ave.100–200 μm	–
GBM Low stress-high T def.	Prcl shape	amoeboid	no evidence of prcl	no evidence of prcl	–	–
	Prcl size	1–2 mm		–	–	–
	Internal def.	- rare undulose ext. - numerous def. lamellaes in intermediate type 4 micro.		–	–	–
	Boundaries	straight	lobate, straight segments	grains pinning around micas	evidence for migrating boundaries	–
	Subgrains	similar to large RX grains	chessboard extinction	–	–	–
	RX grains	amoeboid or polygonal	interfingering	lobate boundaries	–	–
	RX grains size	340 or 90 μm in ave.	220 μm to few mm	ave.120 μm up to 320 μm	–	–

Abbreviations: ave. = average; def. = deformation; ext. = extinction; FZ = fault zone; prcl = porphyroclasts; RX = recrystallized; SZ = shear zone.

time scale of deformation (Burov, 2007). A polymineralic layer has a lower viscosity than a pure layer of quartz, which allows the rock to deform at lower differential stress and induces strain localization (e.g., Herwegh et al., 2011; Speckbacher et al., 2013). Depending on the strain rate during deformation, a single vein may be thoroughly recrystallized or show a strain variation between the margin and the interior (e.g., Trimby et al., 1998), and a thicker vein might show a more homogeneous recrystallization than a thinner one.

The selection of hydrothermal quartz veins for microstructural observation and grain size measurement should therefore be done in order to avoid local mineralogical and stress heterogeneity. The flow stress calculated for quartz vein samples is representative of the vein given that a proper step size is used for the EBSD analysis.

5.2. Comparison of microstructures and flow stress with recrystallized metamorphic rocks

The microstructures that were documented within the samples from the southern Abitibi greenstone belt share numerous characteristics with quartz vein samples in metamorphic rocks documented in the literature (Table 5). A wide variety of textures and DRX mechanisms are found within the samples from this study, compared to other environments of deformation or other rock types. However, the expression of the DRX mechanisms varies from those observed in metamorphic rocks. The size of the largest porphyroclasts is generally much smaller in metamorphic rocks, but this mostly depends on the protolith and its composition (e.g., see Wenk and Christie, 1991; Dunlap et al., 1997; Stipp et al., 2002a; Kidder et al., 2013). In this study, deformation lamellae are documented in samples dominated by SGR or GBM, notably in samples from type 4 microstructures, whereas these textures usually develop in samples dominated by BLG in metamorphic rocks and quartz veins (Table 5). Deformation lamellae, especially basal deformation lamellae, are usually observed in natural samples deformed at temperature <400 °C and at high strain rate deformation creep, (e.g., Trepmann and Stöckhert, 2003; Stipp et al., 2006), although they can also form at low strain rate and at temperature reaching 800 °C (White, 1973; Vernooij and Langenhorst, 2005). The chessboard extinction typical of high temperature subgrain formation, which can form by both basal <a> or prism [c] slip at conditions above ~ 550 °C (Okudaira et al., 1995, 1998; Wallis et al., 2019), was not observed in the Abitibi samples. Similarly, no Dauphiné twins were found during the post-processing of all the samples from this study, although it seems a common feature in mylonites (Stipp and Kunze, 2008; McGinn et al., 2020). This feature was only found locally in orogenic quartz veins from the northeastern part of the Abitibi subprovince (close to the Destor-Porcupine fault zone, Tavares Nassif et al., 2022). These observations suggest that the samples from this study recrystallized at temperatures lower than 550–600 °C, and probably at relatively low to intermediate strain rates compared to quartz-rich metamorphic rocks.

The recrystallized grain size and flow stress calculated from the EBSD data of deformed quartz vein samples as part of this study are within the range of those determined for natural mylonites and quartzites (Fig. 8). The maximum and minimum flow stress values that were calculated for quartz veins are of 103 + 3/-2 MPa and 21.2 + 4.9/-5.4 MPa, respectively, compared to a maximum of 205 + 25/-19 MPa and a minimum of 10 + 4/-2 MPa in quartzite and quartz-rich mica schist (Fig. 8, samples from Behr and Platt, 2011, 2013). The sample GOLD3 of this study, which was interpreted to be recrystallized by GBM, does not lie within the grain size range for GBM taken from Stipp et al. (2010) as a reference for Fig. 8. However, the recrystallized grain size distribution is very wide for this sample (Fig. 3E), and the flow stress calculated for GBM-dominated samples has to be considered as a minimum estimate (Stipp et al., 2010). Other studies found similar grain sizes for samples at the SGR/GBM transition (e.g., Takeshita, 2021). The flow stress recorded in the samples from this study are thus generally low to moderate flow stress values that are comprised in a much narrower range

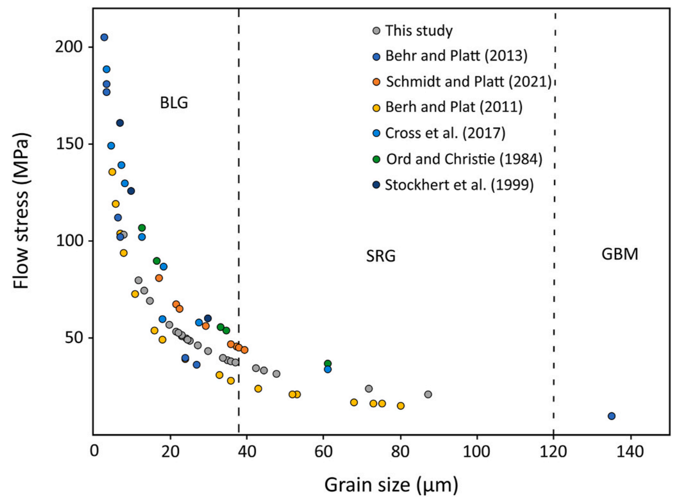

Fig. 8. Plot of the grain size versus the flow stress calculated for recrystallized quartz grains from various studies. Data is derived from several grain sizes quantification methods and flow stress calculated with different piezometers. The flow stresses used for Ord and Christie (1984) and Stöckhert et al. (1999) are the ones calculated with the Twiss (1977) piezometer, as this one was later shown of better accuracy by Stipp et al. (2002b) compared to the other piezometers used in these studies. Transitions between recrystallization mechanisms defined by Stipp et al. (2010) on natural samples, that relates to maximum grain sizes observed for each mechanism, are indicated as a guide. The data from Cross et al. (2017) that allowed to calibrate the piezometer used in this study was also included to compare grain sizes obtained with EBSD to this study's data.

compared to the flow stress recorded in metamorphic rocks (Fig. 8).

5.3. Timing of quartz vein deformation

According to the crack-seal (Ramsay, 1980) and fault-valve (Sibson, 1990; Robert et al., 1995) models, quartz veins form during seismic events, and may deform ductily and recrystallize during aseismic periods. In some cases, the deformation of quartz veins can be almost synchronous with vein development, and the primary microscopic textures of the vein may be preserved (Dowling and Morrison, 1989; Boullier and Robert, 1992; Vearncombe, 1993; Bons et al., 2012). Stress cycles in an orogenic system could cause the recrystallization of the quartz veins as a result of superimposed episodic or continuous strain, after vein formation (Taylor et al., 2021). Additional elements such as pressure fringes or microstylolites indicate internal deformation that occurs during or after the vein formation (Robert and Poulsen, 2001; Bons et al., 2012), or in a previous event of pressure solution (Blenkinsop, 2000; Bons et al., 2012).

The microstructures of quartz vein samples observed in this study demonstrate that ductile deformation and recrystallization has obliterated the primary quartz texture in all but one sample (KL7), and pressure fringes or microstylolites are very rare. Thus, the microstructures undoubtedly formed after the complete vein development. The flow stress calculated by the piezometer should match the peak flow stress associated with the deformation (White et al., 1985), and more importantly it should correspond to the latest ductile deformation event that affected the quartz veins (Kidder et al., 2012, 2016). However, deformation conditions have varied in time and space, depending on the deformation event and the area that was affected by it (Bedeaux et al., 2017). The stress might be localized, and thus the latest deformation event undergone by the quartz veins might not be the same for all veins along the LLCFZ. Moreover, vein formation in the vicinity of the LLCFZ is highly episodic (fault-valve) and concentrated in several events over a period of more than 30 m.y. (Dubé and Mercier-Langevin, 2020). Thus, relating the microstructures and the calculated flow stress to a unique deformation event would be highly speculative.

In addition, the bimodal grain size distribution documented in several samples from the type 3 microstructures indicates that there are probably two groups of recrystallized grains in each of these samples. In these bimodal samples, large porphyroclasts exhibiting internal deformation and shear bands with bulges similar to type 1 microstructures are observed alongside porphyroclasts with evidence of SGR recrystallization. To explain such remaining porphyroclasts, a first stage of BLG-dominated DRX should have been followed by a second stage of SGR-dominated DRX. The reverse appears unlikely, due to the tendency of SGR to form recrystallized grains both within the porphyroclasts and at their boundary. This is also coherent with orogenic quartz vein formation, which may have been formed and later deformed under a prograde metamorphic stage, inducing an increase of the deformation temperature. The dynamically recrystallized grain size dataset for natural samples of Stipp et al. (2010), using 555 samples from 31 studies, do exhibit a bimodal distribution that is correlated to microstructural transitions and thus a change in the dominant DRX mechanism. However, a combination of two coeval recrystallization mechanisms (e.g., Behr and Platt, 2011) cannot explain the bimodal distribution documented within specific samples in this study, as one mechanism is generally dominant in a specific range of strain rate and temperature; although the processes of SGR and GBM operate together to a certain extent (Stipp et al., 2002a).

Alternatively, the bimodal distribution of grain size may be explained by discontinuous deformation of quartz (Urai et al., 1986; Kidder et al., 2016). In metamorphic rocks exhibiting bimodal populations, microstructures formed in a high stress regime overprint low-stress recrystallized grain fabrics (Dunlap et al., 1997; Kidder et al., 2012, 2013; Speckbacher et al., 2013; Price et al., 2016). Similar observations related to uplift and cooling of the host rocks were also made on quartz veins from lode gold deposits (McCuaig and Kerrich, 1998). However, the microstructures in the Abitibi samples suggest a first stage of high flow stress and low temperature deformation (BLG-dominated), followed by a second stage of lower flow stress and higher temperature deformation (SGR-dominated). Thus, the superimposition of two different stress regimes or plastic deformation events may better explain the bimodal distribution (Ord and Christie, 1984; Kolb et al., 2005). This hypothesis is the most coherent one given the microstructures observed in this study and the results of laboratory experimentations on quartz recrystallization. The second and largest population of grains recrystallized by SGR should reliably represent the most recent flow stress experienced by the bimodal samples, as shown by Kidder et al. (2016) on experimentally deformed quartzite.

The bimodal grain size populations documented for some samples in this study highlight important considerations for the timing of the recrystallization. Only four samples (Table 4) exhibit a bimodal grain size distribution and thus probably recorded at least two different stress regimes, whereas most of the samples did not. The most probable explanation is that the quartz veins did not form at the same time even when they belong to a same deposit. This would be coherent with the different vein generations recognized by Robert (1994) in the Val-d'Or district and the age variations measured by Tremblay et al. (2020) on micas in quartz veins hosted by the Bourlamaque pluton. The preservation of primary quartz textures in one sample (sample KL7) indicates that some veins in southern Abitibi greenstone belt probably formed during late increments of veining or were not subjected to superimposed strain allowing conditions for recrystallization.

5.4. Regional implications

The microstructures of the deformed veins in this study should reflect the deformation conditions that prevailed after vein formation in the vicinity of the LLCFZ, given that most quartz vein samples were collected within less than 200 m of the LLCFZ. Providing that recrystallized grain size is independent of temperature (Twiss, 1977; Stipp and Tullis, 2003; Stipp et al., 2006) and that deformation occurred under steady-state conditions, the dominant recrystallization mechanism and the calculated flow stress reflect the range of temperature and the peak flow stress at which quartz vein recrystallization occurred, during the latest plastic deformation along the LLCFZ.

The described microstructures and the EBSD results on the samples that were selected to study the evolution of quartz microstructures with depth at the Goldex and Maritime-Cadillac deposits, indicate both an increase in temperature and a decrease of the flow stress with increasing depth (Fig. 6 and 7). Similar conclusions were obtained by Kidder et al. (2012) on quartzite and quartz veins in various rock types from the Tertiary Taiwan orogen. They show that the flow stress decreases with depth, related to an increase of recrystallized grain size. They determined a flow stress ranging from 200 MPa to 14 MPa for a temperature interval of 250–500 °C and depths of 11–18 km. The results of Kidder et al. (2012) and those of this study on Archean rocks of the Abitibi greenstone belt, are consistent with quartzite flow laws and analog deformation experiments conducted on natural rock samples showing that rheology is in part dependent on temperature, and that an increase in temperature decreases the elastic threshold and the strength of plastically deformed rocks. As such, the differential stress required to maintain plastic deformation and DRX decreases with increasing temperature, which is consistent with the observations made in this study (Figs. 6 and 7).

The microstructures and calculated flow stress for samples collected along the strike of the LLCFZ between the Kirkland Lake and Val d'Or areas also show significant variations (Fig. 9). In the samples from the Kirkland Lake area, quartz exhibits BLG-dominated microstructures implying relatively low temperatures of approximately 280–400 °C (Stipp et al., 2002a, 2002b). These rocks were deformed at relatively high, but variable flow stress conditions (~68.9–103 MPa; Table 2, Fig. 9C), independently of their depth (0–970 m, Fig. 9D). Additionally, the sets of shear bands and fluid inclusion alignment in BLG-dominated samples from this area may indicate that deformation initiated as microcracks in brittle conditions (e.g., van Daalen et al., 1999; Kjøll et al., 2015), although plastic mismatch can also induce microcrack formation (Blenkinsop, 2000). Only one sample from Kirkland Lake (KL4) displays type 3 microstructures dominated by SGR suggesting temperatures high enough to locally allow SGR (Fig. 9A and B). The greenschist facies metamorphism south of the LLCFZ in the Kirkland Lake area suggests a minimum temperature of 300–350 °C, meaning that temperature during late deformation could not have been much higher. In the Rouyn-Noranda area, several samples are dominated by SGR and the flow stress calculated for these samples is generally lower than the one for the Kirkland Lake samples (Table 2, Fig. 9B and C). This suggests that recrystallization occurred at slightly higher temperature (~400°C, Stipp et al., 2002a,b), and at lower flow stress. Samples from the Joannes segment are strictly SGR-dominated and give lower stress values both at surface and at depth (Tables 2 and 3, Fig. 9B,C and D) compared to the other segments of the LLCFZ. The samples at the eastern extremity of the Joannes segment show evidence of GBM, notably at depth (Lapa and Maritime-Cadillac deposits, Fig. 9B and D), indicating locally higher temperatures during plastic deformation. GBM becomes predominant in the Val-d'Or area, as most samples exhibit type 4 microstructures, especially at the Nordeau deposit (450 m depth), which is at the eastern extremity of the Val-d'Or segment of the LLCFZ (Fig. 9A and B). The flow stress recorded by samples on the Val-d'Or segment are comparable to those found on the Malartic segment (Fig. 9B and C).

A possible interpretation of the high flow stress and low temperature microstructures in the west, and low stress and high temperature microstructures in the east of the study area, could be in part related to the erosion level of the crust (e.g., Stöckhert et al., 1999). The western part of the LLCFZ may represent a shallower crustal level relative to the eastern part. This correlates with variations in greenschist metamorphism between the east and west of the fault (Faure et al., 2009).

Regarding the sample depth during deformation, Stipp et al. (2002a)

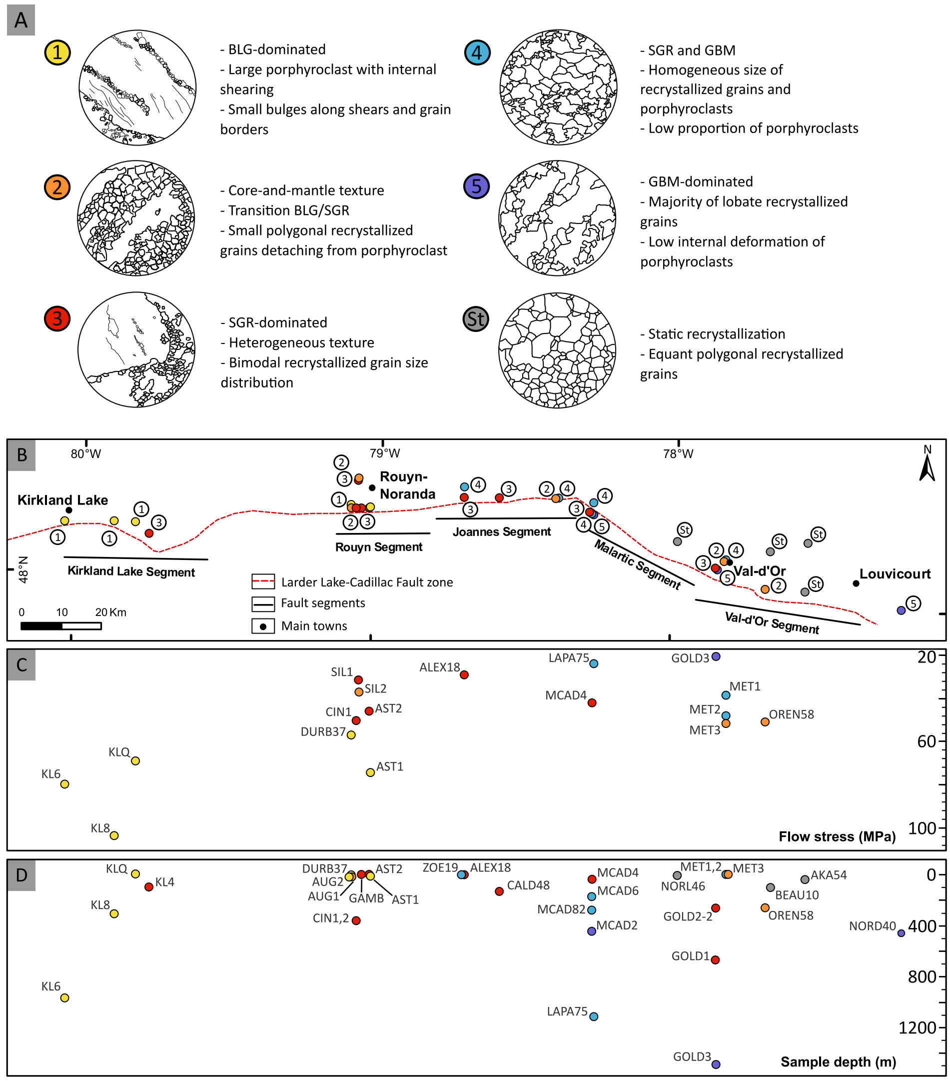

Fig. 9. Summary of the microstructures observed in the studied samples, flow stress calculated from EBSD analysis and original sample depth along the LLCFZ. A. Microstructural types described in part 4.1 of this paper. B. Simplified outline of LLCFZ with location of samples used in this study and corresponding microstructural type number. C. Flow stress calculated from the EBSD data for the selected samples. The position of the point corresponds vertically to the position of the sample along the LLCFZ. Some samples do not have a corresponding flow stress as they were either not analyzed with EBSD, or had a number of recrystallized grains inferior to 427 (see methods for explanations). Note that for samples exhibiting bimodal distribution of recrystallized grain size, the flow stress used is the one calculated for the largest population (Table 4). D. Sample true depth along the LLCFZ. The position of the point corresponds vertically to the position of the sample along the LLCFZ. Note that samples for the Silidor and O'Brien showings are not included as their original depth is unknown.

show that quartz veins in metamorphic rocks are completely recrystallized by GBM above 550 °C. Temperature estimates by Bui et al. (2023) range from 435 °C to 490 °C for samples dominated by GBM, at possibly lower flow stress than those determined for samples from this study. Along with the absence of high-temperature microstructures such as chessboard extinction, this suggest that the temperature reached by the deepest sample from the Goldex deposit (1493m), must have been lower than or close to 550 °C due to its partial recrystallization. For a temperature of about 500 °C during recrystallization, the depth of deformation of the GBM-dominated samples in this study could have been about 20 km using the calculated geotherm at 2.55 Ga by Mareschal and Jaupart (2006). Evidence for ductile behavior of the lower crust during the late Archean (Mareschal and Jaupart, 2006) suggests that quartz veins in Abitibi have formed and later deformed at depth ranging from 10 to 20 km to allow conditions for dynamic recrystallization.

6. Conclusion

The quartz microstructures documented in this study show that hydrothermal quartz veins from orogenic gold deposits of the southern Abitibi greenstone belt are overprinted by DRX microstructures. The microstructures and flow stress recorded by hydrothermal quartz vary locally due to folding and presence of calcite, but these sample-scale variations are less important than the regional-scale ones. The microstructures and flow stress calculated from the mean grain size determined from EBSD data are comparable to those in metamorphic rocks, ranging from 21.2 + 4.9/-5.4 MPa to 103 + 3/-2 MPa. These microstructures reveal that the quartz veins were affected by plastic deformation after their complete crystallization. Samples from several deposits located along the LLCFZ exhibit bimodal recrystallized grain size populations that indicate that the quartz veins recorded at least two distinct plastic deformation events. Regional variations indicate high stress and low temperature deformation in the western part of the

LLCFZ, where samples are dominated by BLG and/or SGR both at surface and at depth, with flow stress ranging from 46.1 + 4.7/-5.9 to 103 + 3/-1 MPa. In the eastern part of the LLCFZ, samples recorded higher temperature and lower flow stress conditions of minimum 21.2 + 4.9/-5.4 MPa. These variations suggest that the western part of the study area exposes a shallower crustal level than the eastern part.

This study shows that analyses and observations commonly used in structural and metamorphic studies can also be applied in the study of auriferous quartz vein formation and deformation in mineral deposits. Recognition of typical quartz DRX textures can be systematized using an end-member chart, as summarized in Fig. 9A. Post-formation processes such as pressure solution and plastic deformation occurring during seismic cycles can impact the morphology and distribution of gold in quartz and sulphides. Hence, the study of quartz microstructures and definition of flow stress in dynamically recrystallized quartz veins appear as a new independent tool for estimating semi-quantitatively the structural and thermal evolution of orogenic gold deposits.

Author Statement

Crystal Brochard: Conceptualization, Investigation, Methodology, Formal analysis, Data curation, Writing - original draft; Writing - review & editing, Visualization.

Michel Jébrak: Conceptualization, Resources, Supervision, Funding acquisition, Writing - review & editing.

Stéphane De Souza: Funding acquisition, Resources, Supervision, Writing - review & editing.

Declaration of competing interest

The authors declare the following financial interests/personal relationships which may be considered as potential competing interests: Crystal Brochard reports financial support was provided by Mitacs Canada.

Data availability

Data will be made available on request.

Acknowledgements

We would like to thank Mohammad Saadati for his help and expertise during the EBSD analyses at the École de technologie supérieure (ÉTS). We are grateful for the discussions with Michael Stipp about dynamic recrystallization, and with Andrew Cross for the EBSD analysis and post-processing of the data during the development of this research project. Many thanks to the Agnico Eagle Mines Ltd. Exploration team, which provided access and sampling of their various properties along the LLCFZ, and for their assistance during the sampling campaign. A special thanks to Alexandre Bernard for the cross section of the Maritime-Cadillac deposit, and Olivier Côté-Mantha for his support thoughout the project. We also thank Michael Higgins, Daniele Pinti and Alain Tremblay who reviewed an early version of this manuscript, which is part of the first author's M.Sc. thesis. Many thanks to the reviewers and the editor who contributed to greatly improve the manuscript through their comments. This work was funded by Mitacs as part of a partnership with Agnico Eagle Mines Ltd, and the analyses supported by the SEG Canada Foundation Award.

Appendix A. Supplementary data

Supplementary data to this article can be found online at https://doi.org/10.1016/j.jsg.2023.104986.

References

Adams, B.L., Wright, S.I., Kunze, K., 1993. Orientation imaging: the emergence of a new microscopy. Metall. Trans. A 24 (4), 819–831.

Bachmann, F., Hielscher, R., Schaeben, H., 2010. Texture analysis with MTEX – free and open source software toolbox. Solid State Phenom. 160, 63–68. https://doi.org/10.4028/www.scientific.net/SSP.160.63.

Bachmann, F., Hielscher, R., Schaeben, H., 2011. Grain detection from 2d and 3d EBSD data-specification of the MTEX algorithm. Ultramicroscopy 111 (12), 1720–1733. https://doi.org/10.1016/j.ultramic.2011.08.002.

Barbe, P., 2011. Caractérisation d'une minéralisation aurifère centrée sur une brèche intrusive, propriété Dubuisson, Val-d'Or, Québec, Canada. M.Sc. Thesis, Université du Québec à Chicoutimi.

Beauregard, A.-J., Gaudreault, D., D'Amours, C., 2012. NI 43-101 Technical Report of the Akasaba Property, Geologica. GM66680. Ministère de l'Énergie et des Ressources naturelles.

Beausoleil, C., 2018. NI 43-101 Technical Report and Mineral Resource Estimate for the O'Brien Project, Abitibi, Québec. InnovExplo (for Radisson Mining Resources Inc.

Bedeaux, P., Mathieu, L., Pilote, P., Rafini, S., Daigneault, R., 2018. Origin of the Piché structural complex and implications for the early evolution of the archean crustal-scale cadillac – Larder Lake fault zone, Canada. Can. J. Earth Sci. 55 (8), 905–922.

Bedeaux, P., Pilote, P., Daigneault, R., Rafini, S., 2017. Synthesis of the structural evolution and associated gold mineralization of the Cadillac Fault, Abitibi, Canada. Ore Geol. Rev. 82, 49–69. https://doi.org/10.1016/j.oregeorev.2016.11.029.

Behr, W.M., Platt, J.P., 2011. A naturally constrained stress profile through the middle crust in an extensional terrane. Earth Planet Sci. Lett. 303 (3–4), 181–192. https://doi.org/10.1016/j.epsl.2010.11.044.

Behr, W.M., Platt, J.P., 2013. Rheological evolution of a Mediterranean subduction complex. J. Struct. Geol. 54, 136–155. https://doi.org/10.1016/j.jsg.2013.07.012.

Belzile, E., 2016. Updated Mineral Resource Technical Report: Marban Block Property, Québec, Canada. Belzile Solutions Inc (On behalf of Osisko Mining Inc.

Benn, K., Peschler, A.P., 2005. A detachment fold model for fault zones in the Late Archean Abitibi greenstone belt. Tectonophysics 400 (1–4), 85–104. https://doi.org/10.1016/j.tecto.2005.02.011.

Bernard, A., 2018. Campagne de forage, propriété Maritime-Cadillac (PN-141), hiver 2017/hiver 2018 Agnico-Eagle Mines Limited. GM70997, Ministère de l'Énergie et des Ressources naturelles.

Bestmann, M., Piazolo, S., Spiers, C.J., Prior, D.J., 2005. Microstructural evolution during initial stages of static recovery and recrystallization: new insights from in-situ heating experiments combined with electron backscatter diffraction analysis. J. Struct. Geol. 27 (3), 447–457. https://doi.org/10.1016/j.jsg.2004.10.006.

Blenkinsop, T.G., 2000. Deformation Microstructures and Mechanisms in Minerals and Rocks. Springer, Netherlands.

Bons, P.D., Elburg, M.A., Gomez-Rivas, E., 2012. A review of the formation of tectonic veins and their microstructures. J. Struct. Geol. 43, 33–62. https://doi.org/10.1016/j.jsg.2012.07.005.

Boullier, A.-M., Robert, F., 1992. Palaeoseismic events recorded in Archaean gold-quartz vein networks, Val d'Or, Abitibi, Quebec, Canada. J. Struct. Geol. 14 (2), 161–179.

Bourgault, E., Boudrias, G., 2013. Travaux d'exploration Janvier 2009 - Décembre 2010 Propriété Joanna Hecla Québec Inc. GM 68044, Ministère de l'Énergie et des Ressources naturelles.

Brochard, Crystal, 2022. Paléo-contraintes et origine des fluides des veines orogéniques de la ceinture de roches vertes de l'Abitibi. M.Sc. Thesis. Université du Québec à Montréal.

Bui, D.V., Takeshita, T., Ando, J.-i., Yamamoto, T., Huang, W., Yeo, T., et al., 2023. Development of the Median Tectonic Line-related shear zone, southwest Japan: an analysis of strain localization processes. Tectonophysics 850, 229–751.

Burov, E.B., 2007. Plate rheology and mechanics. In: Schubert, G. (Ed.), Treatise on Geophysics. Elsevier, Amsterdam, pp. 99–151.

Card, K.D., 1990. A review of the superior province of the Canadian shield, a product of archean accretion. Precambrian Res. 48, 99–156.

Carrier, A., Jébrak, M., Angelier, J., Holyland, P., 2000. The Silidor deposit, Rouyn-Noranda district, Abitibi belt: geology, structural evolution, and paleostress modeling of an Au quartz vein-type deposit in an Archean Trondhjemite. Econ. Geol. 95 (5), 1049–1065. https://doi.org/10.2113/gsecongeo.95.5.1049.

Chapon, B., 2017. Travaux 2016-2017 effectués sur la propriété Rouyn Yorbeau Resources Inc. (GM 70530): Ministère de l'Énergie et des Ressources naturelles.

Clarke, C., 2016. 2016 Skead-MacGregor Prospecting Program - Kirkland Lake Project Canadian Malartic Corporation. Ontario Ministry of Northern Development, Mines, Natural Resources and Forestry.

Cotton, R., 2006. Geometric Standard Deviation. MATLAB Central File Exchange. From. https://www.mathworks.com/matlabcentral/fileexchange/10397-geometric-standard-deviation.

Couture, J.-F., Pilote, P., Machado, N., Desrochers, J.-P., 1994. Timing of gold mineralization in the Val-d'Or District, southern Abitibi Belt: evidence for two distinct mineralizing events. Econ. Geol. 89, 1542–1.551.

Cross, A.J., Prior, D.J., Stipp, M., Kidder, S., 2017. The recrystallized grain size piezometer for quartz: an EBSD-based calibration. Geophys. Res. Lett. 44 (13), 6667–6674. https://doi.org/10.1002/2017gl073836.

Daigneault, R., Mueller, W.U., Chown, E.H., 2002. Oblique Archean subduction: accretion and exhumation of an oceanic arc during dextral transpression, Southern Volcanic Zone, Abitibi Subprovince Canada. Precambrian Res. 115, 261–290.

Daigneault, R., Mueller, W.U., Chown, E.H., 2004. Abitibi greenstone belt plate tectonics: the diachronous history of arc development, accretion and collision. In: Eriksson, P. G., Altermann, W., Nelson, D.R., Mueller, W.U., Catuneanu, O. (Eds.), The Precambrian Earth: Tempos and Events. Elsevier, Amsterdam, pp. 88–103.

Dowling, K., Morrison, G., 1989. Application of quartz textures to the classification of gold deposits using north queensland examples. In: Keays, R.R., Ramsay, W.R.H., Groves, D.I. (Eds.), The Geology of Gold Deposits: the Perspective in 1988. Society of Economic Geology, pp. 342–355.

Drury, M.R., Urai, J.L., 1990. Deformation-related recrystallization processes. Tectonophysics 172 (3–4), 235–253. https://doi.org/10.1016/0040-1951(90)90033-5.

Dubé, B., Mercier-Langevin, P., 2020. Gold Deposits of the Archean Abitibi Greenstone Belt, Canada, vol. 23. SEG Special publications, pp. 669–708.

Dunlap, W.J., Hirth, G., Teyssier, C., 1997. Thermomechanical evolution of a ductile duplex. Tectonics 16 (6), 983–1000. https://doi.org/10.1029/97TC00614.

Faure, S., 2015. Relations entre les minéralisations aurifères et les isogrades métamorphiques en Abitibi. Rapport du CONSOREM 2013-03, 52.

Faure, S., Rafini, S., Trépanier, S., 2009. Paléopressions, perméabilité crustale et hydrothermalisme : implications pour les minéralisations aurifères orogéniques en Abitibi. Rapport du Consorem 2008–01, 26.

Fougerouse, D., Micklethwaite, S., Tomkins, A.G., Mei, Y., Kilburn, M., Guagliardo, P., Fisher, L.A., Halfpenny, A., Gee, M., Paterson, D., Howard, D.L., 2016. Gold remobilisation and formation of high grade ore shoots driven by dissolution-reprecipitation replacement and Ni substitution into auriferous arsenopyrite. Geochem. Cosmochim. Acta 178, 143–159. https://doi.org/10.1016/j.gca.2016.01.040.

Genest, R., Lagueux, J.-F., Robichaud, F., Boily, S., 2012. Technical Report on Production of the M and E Zones at Goldex Mine. Agnico-Eagle Mines Limited.

Gifkins, R.C., 1994. Grain-boundary participation in high-temperature deformation: an historical review. Mater. Char. 32 (2), 59–77. https://doi.org/10.1016/1044-5803(94)90093-0.

Goldfarb, R.J., Baker, T., Dubé, B., Groves, D.I., Hart, C.R.J., Gosselin, P., 2005. Distribution, Character, and Genesis of Gold Deposits in Metamorphic Terranes. Economic Geology, 100th Anniversary, pp. 407–450.

Gottstein, G., Mecking, H., 1985. Recrystallization. In: Wenk, Dans H.-R (Ed.), Preferred Orientation in Deformed Metals and Rocks: an Introduction to Modern Texture Analysis. Academic Press Inc.

Halfpenny, A., Prior, D.J., Wheeler, J., 2012. Electron backscatter diffraction analysis to determine the mechanisms that operated during dynamic recrystallisation of quartz-rich rocks. J. Struct. Geol. 36, 2–15. https://doi.org/10.1016/j.jsg.2012.01.001.

Herwegh, M., Linckens, J., Ebert, A., Berger, A., Brodhag, S.H., 2011. The role of second phases for controlling microstructural evolution in polymineralic rocks: a review. J. Struct. Geol. 33 (12), 1728–1750. https://doi.org/10.1016/j.jsg.2011.08.011.

Higgins, M.D., 2000. Measurement of crystal size distributions. Am. Mineral. 85 (9), 1105–1116. https://doi.org/10.2138/am-2000-8-901.

Higgins, M.D., 2006. Quantitative Textural Measurements in Igneous and Metamorphic Petrology. Cambridge University Press, UK.

Humphreys, F.J., Hatherly, M., 2004. Recrystallization and Related Annealing Phenomena, second ed. Elsever, Netherlands.

Hunt, L., Rubingh, K.E., 2018. Preliminary results from mapping alteration and structure of a new exposure south of dobie, Ontario. In: Summary of field work and other activities, Ontario Geol. Surv., pp. 1–6, 2018 (42).

Hunter, N.J.R., Voisey, C.R., Tomkins, A.G., Wilson, C.J.L., Luzin, V., Stephen, N.R., 2021. Deformation mechanisms in orogenic gold systems during aseismic periods: microstructural evidence from the central victorian gold deposits, southeast Australia. Econ. Geol. 116 (8), 1849–1864. https://doi.org/10.5382/econgeo.4885.

Ispolatov, V., Lafrance, B., Dubé, B., Creaser, R., Hamilton, M., 2008. Geologic and structural setting of gold mineralization in the Kirkland Lake-Larder Lake gold belt, Ontario. Econ. Geol. 103, 1309–1340.

Kidder, S., Avouac, J.-P., Chan, Y.-C., 2012. Constraints from rocks in the Taiwan orogen on crustal stress levels and rheology. J. Geophys. Res. Solid Earth 117 (B9). https://doi.org/10.1029/2012JB009303.

Kidder, S., Avouac, J.P., Chan, Y.C., 2013. Application of titanium-in-quartz thermobarometry to greenschist facies veins and recrystallized quartzites in the Hsüehshan range, Taiwan. Solid Earth 4 (1), 1–21. https://doi.org/10.5194/se-4-1-2013.

Kidder, S., Hirth, G., Avouac, J.-P., Behr, W., 2016. The influence of stress history on the grain size and microstructure of experimentally deformed quartzite. J. Struct. Geol. 83, 194–206. https://doi.org/10.1016/j.jsg.2015.12.004.

Kjøll, H.J., Viola, G., Menegon, L., Sørensen, B.E., 2015. Brittle–viscous deformation of vein quartz under fluid-rich lower greenschist facies conditions. Solid Earth 6 (2), 681–699. https://doi.org/10.5194/se-6-681-2015.

Kolb, J., Rogers, A., Meyer, F., Siemes, H., 2005. Dominant coaxial deformation of veins during the interseismic stage of the fault-valve cycle: microfabrics of laminated quartz veins of the Hutti gold mine, India. J. Struct. Geol. 27, 2043–2057. https://doi.org/10.1016/j.jsg.2005.06.005.

Kramo, K.B., 2017. Rapport de campagne de forage, automne 2016. propriété Bousquet-Odyno IAMGOLD Corporation (GM 70826).

Lafrance, B., 2015. Geology of the orogenic Cheminis gold deposit along the Larder Lake – cadillac deformation zone, Ontario. Can. J. Earth Sci. 52 (12), 1093–1108. https://doi.org/10.1139/cjes-2015-0067.

Langton, J., Horvath, A.S., 2009. Technical Report. Nordeau Gold Mineral Properties MRB & Associates. GM 64504, Ministère de l'Énergie et des Ressources naturelles.

Langton, J., Ladid, A., 2019. Val-d'Or, québec. In: NI-43-101 Technical Report and Mineral Resource Estimate: East-Cadillac Gold Project. MRB & Associates.

Laporte, J., 2016. Mineralogical Study of the Auriferous Shear Zone along the Augmitto-Astoria Segment in the Cadillac Break South to Rouyn-Noranda, Abitibi. Université du Québec à Montréal, Québec. M.Sc. Thesis.

Lemarchand, J., 2012. Les minéralisations filoniennes aurifères du pluton de Bourlamaque (Val-d'Or, Abitibi): Synthèse structurale et apports de la datation 40Ar/39Ar. Ph.D. Thesis. Université de Renne 1 - Université Du Québec à Montréal.

Limpert, E., Stahel, W.A., Abbt, M., 2001. Log-normal distributions across the sciences: keys and clues. Bioscience 51 (5).

Lloyd, G.E., 1987. Atomic number and crystallographic contrast images with the SEM: a review of backscattered electron techniques. Mineral. Mag. 51, 3–19.

Lopez-Sanchez, M.A., Llana-Fúnez, S., 2015. An evaluation of different measures of dynamically recrystallized grain size for paleopiezometry or paleowattometry studies. Solid Earth 6 (2), 475–495. https://doi.org/10.5194/se-6-475-2015.

Lopez-Sanchez, M.A., Llana-Fúnez, S., 2016. An extension of the Saltykov method to quantify 3D grain size distributions in mylonites. J. Struct. Geol. 93, 149–161. https://doi.org/10.1016/j.jsg.2016.10.008.

Lopez-Sanchez, M.A., 2020. Which average, how many grains, and how to estimate robust confidence intervals in unimodal grain size populations. J. Struct. Geol. 135 https://doi.org/10.1016/j.jsg.2020.104042.

Lychagin, D.V., Kungulova, E.N., Moskvichev, E.N., Tomilenko, A.A., Tishin, P.A., 2020. Microstructure of vein quartz aggregates as an indicator of their deformation history: an example of vein systems from western transbaikalia (Russia). Minerals 10, 865. https://doi.org/10.3390/min10100865.

Mareschal, J.-C., Jaupart, C., 2006. In: Benn, K., Mareschal, J.C., Condie, K.C. (Eds.), Archean Geodynamics and Environments, 164. American Geophysical Union, pp. 61–73.

Masson, M.W., 2017. 2017 Assessment Report on the Amalgamated Kirkland Property Canadian Malartic Corporation. Ontario Ministry of Northern Development, Mines, Natural Resources and Forestry.

McCuaig, T.C., Kerrich, R., 1998. P-T-t-deformation-fluid characteristics of lode gold deposits: evidence from alteration systematics. Ore Geol. Rev. 12 (6), 381–453. https://doi.org/10.1016/S0169-1368(98)80002-4.

McGinn, C., Miranda, E.A., Hufford, L.J., 2020. The effects of quartz Dauphiné twinning on strain localization in a mid-crustal shear zone. J. Struct. Geol. 134, 103980 https://doi.org/10.1016/j.jsg.2020.103980.

Mueller, W.U., Daigneault, R., Mortensen, J.K., Chown, E.H., 1996. Archean terrane docking: upper crust collision tectonics, Abitibi greenstone belt, Quebec, Canada. Tectonophysics 265, 127–150.

Munger, A., 2019. Facteurs de contrôle et organisation des filons aurifères orogéniques du gisemement de Goldex, Val-d'Or. Université du Québec à Chicoutimi, Québec. M. Sc. Thesis.

Neumayr, P., Hagemann, S.G., Couture, J.F., 2000. Structural setting, textures, and timing of hydrothermal vein systems in the Val d'Or camp, Abitibi, Canada: implications for the evolution of transcrustal, second- and third-order fault zones and gold mineralization. Can. J. Earth Sci. 37 (1), 95–114. https://doi.org/10.1139/e99-105.

Okudaira, T., Takeshita, T., Hara, I., Ando, J.-i., 1995. A new estimate of the conditions for transition from basal <a> to prism [c] slip in naturally deformed quartz. Tectonophysics 250 (1), 31–46. https://doi.org/10.1016/0040-1951(95)00039-4.

Okudaira, T., Takeshita, T., Toriumi, M., 1998. Prism- and basal-plane parallel subgrain boundaries in quartz: a microstructural geothermobarometer. J. Metamorph. Geol. 16 (1), 141–146. https://doi.org/10.1111/j.1525-1314.1998.00063.x.

Ord, A., Christie, J.M., 1984. Flow stresses from microstructures in mylonitic quartzites of the Moine Thrust zone, Assynt area, Scotland. J. Struct. Geol. 6 (6), 639–654.

Platt, J.P., Behr, W.M., 2011. Grainsize evolution in ductile shear zones: implications for strain localization and the strength of the lithosphere. J. Struct. Geol. 33 (4), 537–550. https://doi.org/10.1016/j.jsg.2011.01.018.

Ploeger, F.R., 2015. Assessment Report for Diamond Drilling on the Canadian Kirkland Property of Canadian Malartic Corporation, Lebel Township, District of Timiskaming Canadian Malartic Corporation. Ontario Ministry of Northern Development, Mines, Natural Resources and Forestry.

Poulsen, H., 2017. The Larder LakeLake-Cadillac break and its gold disctricts. Rev. Econ. Geol. 19, 133–167.

Powell, W.G., Carmichael, D.M., Hodgson, C.J., 1995. Conditions and timing of metamorphism in the southern Abitibi greenstone belt, Quebec. Can. J. Earth Sci. 32 (6), 787–805. https://doi.org/10.1139/e95-067.

Price, N.A., Song, W.J., Johnson, S.E., Gerbi, C.C., Beane, R.J., West, D.P., 2016. Recrystallization fabrics of sheared quartz veins with a strong pre-existing crystallographic preferred orientation from a seismogenic shear zone. Tectonophysics 682, 214–236. https://doi.org/10.1016/j.tecto.2016.05.030.

Prior, D.J., Mariani, E., Wheeler, J., 2009. EBSD in the earth sciences: applications, common practice, and challenges. In: Schwartz, A., Kumar, M., Adams, B., Field, D. (Eds.), Electron Backscatter Diffraction in Materials Science. Springer, Boston, MA, pp. 345–360.

Ramsay, J.G., 1980. The crack–seal mechanism of rock deformation. Nature 284 (5752), 135–139. https://doi.org/10.1038/284135a0.

Ramsay, J.G., Huber, M.I., 1983. Strain Analysis). In: Techniques of Modern Structural Geology, vol. 1. Academic Press, London.

Rezeau, H., Moritz, R., Beaudoin, G., 2017. Formation of Archean batholith-hosted gold veins at the Lac Herbin deposit, Val-d'Or district, Canada: Mineralogical and fluid inclusion constraints. Miner Deposita 52, 421–442. https://doi.org/10.1007/s00126-016-0669-5.

Robert, F., 1994. Vein fields in gold districts: the example of Val d'Or, southeastern Abitibi subprovince, Quebec. In: Current Research 1994-C. Geological Survey of Canada, pp. 295–302.

Robert, F., Boullier, A.-M., Firdaous, K., 1995. Gold-quartz veins in metamorphic terranes and their bearing on the role of fluids in faulting. J. Geophys. Res. Solid Earth 100 (B7), 12861–12879. https://doi.org/10.1029/95jb00190.

Robert, F., Brown, A.C., 1986a. Archean gold-bearing quartz veins at the sigma mine, Abitibi greenstone belt, Quebec: Part I. Geologic relations and formation of the vein system. Econ. Geol. 81, 578–592.
Robert, F., Brown, A.C., 1986b. Archean gold-bearing quartz veins at the sigma mine, Abitibi greenstone belt, Quebec: Part II. Vein paragenesis and hydrothermal alteration. Econ. Geol. 81, 593–616.
Robert, F., Poulsen, H., 2001. Vein Formation and deformation in greenstone gold deposits. In: Richards, J.P., Tosdal, R.M. (Eds.), Structural Controls on Ore Genesis, Reviews in Economic Geology, vol. 14, pp. 111–152.
Robert, F., Poulsen, H., Cassidy, K.F., Hodgson, C.J., 2005. Gold Metallogeny of the Superior and Yilgarn Cratons. Economic Geology 100th Anniversary, pp. 1001–1033.
Savard, C., Carrier, A., Durieux, G., 2018. NI 43-101 Technical Report and Updated Mineral Resource Estimate for the Orenada Zones 2 and 4 Project, Orenada Group Properties, InnovExplo (For Alexandria Minerals Corporation).
Schmatz, J., Urai, J.L., 2011. The interaction of migrating grain boundaries and fluid inclusions in naturally deformed quartz: a case study of a folded and partly recrystallized quartz vein from the Hunsrück Slate, Germany. J. Struct. Geol. 33 (4), 468–480. https://doi.org/10.1016/j.jsg.2010.12.010.
Shigematsu, N., Prior, D.J., Wheeler, J., 2006. First combined electron backscatter diffraction and transmission electron microscopy study of grain boundary structure of deformed quartzite. J. Microsc. 224, 306–321.
Sibson, R.H., 1990. Conditions for fault-valve behaviour. Geological Society, London, Special Publications 54 (1), 15. https://doi.org/10.1144/GSL.SP.1990.054.01.02.
Simard, M., Gaboury, D., Daigneault, R., Mercier-Langevin, P., 2013. Multistage gold mineralization at the Lapa mine, Abitibi subprovince: insights into auriferous hydrothermal and metasomatic processes in the cadillac–larder lake fault zone. Miner. Deposita 48 (7), 883–905. https://doi.org/10.1007/s00126-013-0466-3.
Speckbacher, R., Stipp, M., Behrmann, J.H., Heidelbach, F., 2013. Fluid-assisted fracturing, cataclasis, and resulting plastic flow in mylonites from the Moresby Seamount detachment, Woodlark Basin. J. Struct. Geol. 56, 156–171. https://doi.org/10.1016/j.jsg.2013.10.001.
Stevenson, D.B., Broughton, D.W., Cruji, D.R., Masson, M.W., Parry, S.E., 1995. Geology and exploration history of the amalgamated Kirkland deposit, Kirkland Lake, Ontario. Explor. Min. Geol. 4 (3).
Stipp, M., Stünitz, H., Heilbronner, R., Schmid, S.M., 2002a. Dynamic Recrystallization of Quartz: Correlation between Natural and Experimental Conditions, vol. 200. Geological Society London Special Publications, pp. 171–190.
Stipp, M., Stünitz, H., Heilbronner, R., Schmid, S.M., 2002b. The eastern Tonale fault zone: a 'natural laboratory' for crystal plastic deformation of quartz over a temperature range from 250 to 700°C. J. Struct. Geol. 24, 1861–1884.
Stipp, M., Tullis, J., 2003. The recrystallized grain size piezometer for quartz. Geophys. Res. Lett. 30 (21) https://doi.org/10.1029/2003gl018444.
Stipp, M., Tullis, J., Behrens, H., 2006. Effect of water on the dislocation creep microstructure and flow stress of quartz and implications for the recrystallized grain size piezometer. J. Geophys. Res. 111 (B4) https://doi.org/10.1029/2005jb003852.
Stipp, M., Kunze, K., 2008. Dynamic recrystallization near the brittle-plastic transition in naturally and experimentally deformed quartz aggregates. Tectonophysics 448 (1–4), 77–97. https://doi.org/10.1016/j.tecto.2007.11.041.
Stipp, M., Tullis, J., Scherwath, M., Behrmann, J.H., 2010. A new perspective on paleopiezometry: dynamically recrystallized grain size distributions indicate mechanism changes. Geology 38 (8), 759–762. https://doi.org/10.1130/g31162.1.
Stöckhert, B., Brix, M.R., Kleinschrodt, R., Hurford, A.J., Wirth, R., 1999. Thermochronometry and microstructures of quartz—a comparison with experimental flow laws and predictions on the temperature of the brittle–plastic transition. J. Struct. Geol. 21 (3), 351–369. https://doi.org/10.1016/S0191-8141(98)00114-X.
Takeshita, T., 2021. Quartz microstructures from the sambagawa metamorphic rocks, southwest Japan: indicators of deformation conditions during exhumation. Minerals 11 (10). https://doi.org/10.3390/min11101038.
Tavares Nassif, M., Monecke, T., Reynolds, T.J., Kuiper, Y.D., Goldfarb, R.J., Piazolo, S., Lowers, H.A., 2022. Formation of orogenic gold deposits by progressive movement of a fault-fracture mesh through the upper crustal brittle-ductile transition zone. Sci. Rep. 12, 17379.
Taylor, R.D., Monecke, T., Reynolds, T.J., Monecke, J., 2021. Paragenesis of an orogenic gold deposit: new insights on mineralizing processes at the grass valley district, California. Econ. Geol. 116 (2), 323–356. https://doi.org/10.5382/econgeo.4794.
Théberge, L., 2011. Campagne de forage 2010 Propriété Maritime Cadillac (PN-141) Canton Cadillac, Abitibi, Québec Agnico-Eagle Mines Limited. Ministère de l'Énergie et des Ressources naturelles. GM 65770.
Tremblay, A., Ruffet, G., Lemarchand, J., 2020. Timing and duration of Archean orogenic gold deposits in the Bourlamaque pluton, Val d'Or mining camp, Abitibi, Canada. Ore Geol. Rev. 127 https://doi.org/10.1016/j.oregeorev.2020.103812.
Tremblay, D., 2007. Rapport des travaux de sondage du 16 Décembre 2005 au 11 Janvier 2007 Yorbeau Resources Inc. GM 63145. Ministère de l'Énergie et des Ressources naturelles.
Trepmann, C.A., Stöckhert, B., 2003. Quartz microstructures developed during non-steady state plastic flow at rapidly decaying stress and strain rate. J. Struct. Geol. 25 (12), 2035–2051. https://doi.org/10.1016/S0191-8141(03)00073-7.
Trepmann, C.A., Seybold, L., 2019. Deformation at low and high stress-loading rates. Geosc. Front. 10 (1), 43–54. https://doi.org/10.1016/j.gsf.2018.05.002.
Trepmann, C.A., Stöckhert, B., 2009. Microfabric of folded quartz veins in metagreywackes: dislocation creep and subgrain rotation at high stress. J. Meta. Geol. 27 (8), 555–570. https://doi.org/10.1111/j.1525-1314.2009.00842.x.
Trimby, P.W., Prior, D.J., 1999. Microstructural imaging techniques: a comparison between light and scanning electron microscopy. Tectonophysics 301, 71–81.
Trimby, P.W., Prior, D.J., Wheeler, J., 1998. Grain boundary hierarchy development in a quartz mylonite. J. Struct. Geol. 20 (7), 917–935.
Tuba, G., Kontak, D.J., Choquette, B.G., Pfister, J., Hastie, E.C.G., van Hees, E.H.P., 2021. Fluid diversity in the gold-endowed Archean orogenic systems of the Abitibi greenstone belt (Canada) I: constraining the PTX of prolonged hydrothermal systems. Ore Geol. Rev. 135 https://doi.org/10.1016/j.oregeorev.2021.104221.
Twiss, R.J., 1977. Theory and applicability of a recrystallized grain size paleopiezometer. In: M, W. (Ed.), Stress in the Earth. Birkhäuser, Basel, pp. 227–244.
Urai, J.L., Means, W.D., Lister, G.S., 1986. Dynamic recrystallisation of minerals. In: Hobbs, Dans B.E., Heard, H.C. (Eds.), Mineral and Rock Deformation, vol. 36. Laboratory Studies, pp. 161–199.
van Daalen, M., Heilbronner, R., Kunze, K., 1999. Orientation analysis of localized shear deformation in quartz fibres at the brittle-ductile transition. Tectonophysics 303, 83–107.
Vearncombe, J.R., 1993. Quartz vein morphology and implications for formation depth and classification of Archaean gold-vein deposits. Ore Geol. Rev. 8 (5), 407–424. https://doi.org/10.1016/0169-1368(93)90036-X.
Vernooij, M.G.C., Langenhorst, F., 2005. Experimental reproduction of tectonic deformation lamellae in quartz and comparison to shock-induced planar deformation features. Meteoritics Planet Sci. 40 (9–10), 1353–1361. https://doi.org/10.1111/j.1945-5100.2005.tb00406.x.
Vollbrecht, A., Stipp, M., Olesen, N.Ø., 1999. Crystallographic orientation of microcracks in quartz and inferred deformation processes: a study on gneisses from the German Continental Deep Drilling Project (KTB). Tectonophysics 303 (1), 279–297. https://doi.org/10.1016/S0040-1951(98)00265-0.
White, S., 1973. Deformation lamellae in naturally deformed quartz. Nat. Phys. Sci. (Lond.) 245 (141), 26–28. https://doi.org/10.1038/physci245026a0.
White, S.H., 1976. The effects of strain on microstructures, fabrics and deformation mechanisms in quartzites. Phil. Trans. Roy. Soc. Lond. Math. Phys. Sci. 283, 69–86.
White, S.H., Drury, M.R., Ion, S.E., Humphreys, F.J., 1985. Large strain deformation studies using polycrystalline magnesium as a rock analogue. Part I: grain size paleopiezometry in mylonite zones. Phys. Earth Planet. In. 40 (3), 201–207. https://doi.org/10.1016/0031-9201(85)90130-X.
Wallis, D., Parsons, A.J., Hansen, L.N., 2019. Quantifying geometrically necessary dislocations in quartz using HR-EBSD: Application to chessboard subgrain boundaries. J. Struct. Geol. 125, 235–247.
Wenk, H.-R., Christie, J.M., 1991. Comments on the interpretation of deformation textures in rocks. J. Struct. Geol. 13 (10), 1091–1110.
White, W.H., 1943. The mechanism and environment of gold deposition in veins [North America]. Econ. Geol. 38 (6), 512–532. https://doi.org/10.2113/gsecongeo.38.6.512.
Wilkinson, L., Cruden, A.R., Krogh, T.E., 1999. Timing and kinematics of post-Timiskaming deformation within the Larder Lake - cadillac deformation zone, southwest Abitibi greenstone belt, Ontario, Canada. Can. J. Earth Sci. 36 (4), 627–647. https://doi.org/10.1139/e99-015.